

A Unified Variational Functional for Equidistribution and Alignment in Moving Mesh Adaptation

Wenbin Wang¹, Yunqing Huang², and Huayi Wei^{*3}

¹Hunan Research Center of the Basic Discipline Fundamental Algorithmic Theory and Novel Computational Methods, Xiangtan University, Xiangtan 411105, Hunan, China

²Hunan International Scientific and Technological Innovation Cooperation Base of Computational Science, Key Laboratory of Intelligent Computing and Information Processing of Ministry of Education, Xiangtan University, Xiangtan 411105, Hunan, China

³National Center of Applied Mathematics in Hunan, Hunan Key Laboratory for Computation and Simulation in Science and Engineering, Xiangtan 411105, Hunan, China

ABSTRACT

Existing variational mesh functionals often suffer from strong nonlinearity or dependence on empirical parameters. We propose a new variational functional for adaptive moving mesh generation that enforces equidistribution and alignment through an A -pullback formulation, where $A = J^{-1}M^{-1}J^{-T}$. The functional combines a trace-based term with a logarithmic determinant term, achieving balanced control of mesh size and anisotropy without empirical parameters. We establish coercivity, polyconvexity, existence of minimizers, and geodesic convexity with respect to the inverse Jacobian, and derive a simplified geometric discretization leading to an efficient moving mesh algorithm. Numerical experiments confirm the theoretical properties and demonstrate robust adaptive behavior for function-induced meshes and Rayleigh-Taylor instability simulations.

Keywords variational moving mesh ,adaptive mesh generation ,equidistribution, alignment,geometric discretization ,MMPDE

MSC codes: 65M50, 65N50

1 Introduction

Moving mesh methods have been extensively developed and widely applied to fluid dynamics, heat transfer, combustion modeling, and related fields [27, 28, 23, 26]. They are particularly effective for problems with localized solution features—such as shock waves and boundary layers—where fixed mesh methods would require global refinement and incur unnecessary computational costs. By dynamically redistributing mesh points according to solution features without altering mesh topology, moving mesh methods achieve superior efficiency and accuracy compared to static adaptive approaches. Their practical value has been well-established through extensive numerical studies.

Among various approaches, variational moving mesh methods have garnered considerable attention. A substantial body of work has advanced these methods from a variational perspective, demonstrating their effectiveness in solving partial differential equations [14, 5, 19, 18, 30, 6]. Variational mesh adaptation represents a specific class of anisotropic mesh adaptation; see [25, 29, 1, 16] for related contributions. In particular, techniques based on anisotropic centroidal Voronoi tessellations (ACVT) and natural metrics have been developed to construct suitable metric tensors for anisotropic elliptic problems [16].

*Corresponding author.

The central concept of variational mesh adaptation is to construct a mesh functional incorporating equidistribution and alignment, whose minimization yields an elliptic mesh generation system. This approach offers several advantages: the elliptic nature ensures smooth meshes; it provides flexibility to systematically integrate diverse adaptive criteria into a unified energy functional; and it allows exact specification of boundary correspondence—critical for complex geometries. Building on Huang’s foundational work [10, 14], which established the equidistribution and alignment conditions as geometric and physically motivated principles, subsequent functionals have progressively refined these concepts.

Despite these advances, designing a functional that simultaneously achieves equidistribution, stable alignment, and favorable analytical properties remains challenging. While Huang’s framework [12] provides geometric consistency, simplifying implementation and enhancing robustness and Kolasinski-Huang’s approach [20] eliminates empirical parameters through the Frobenius norm. Both encounter drawbacks: the former introduces empirical weights, while the latter exhibits excessive nonlinearity that deteriorates convergence under high metric anisotropy or stiffness. These complementary limitations motivate the development of a new functional that inherits the best features of both approaches—parameter-free formulation with controlled nonlinearity—while maintaining robust equidistribution and alignment properties.

In this work, we propose a new variational functional that alleviates excessive nonlinearity and multi-parameter dependence while strictly maintaining equidistribution and alignment. The key innovation is an \mathbf{A} -pullback formulation—where $\mathbf{A} = \mathbf{J}^{-1} \mathbf{M}^{-1} \mathbf{J}^{-T}$ —combined with a trace-based term and a logarithmic determinant term. We establish several key analytical properties, including coercivity, polyconvexity, and geodesic convexity with respect to the inverse Jacobian. At the discrete level, we derive a simplified geometric discretization that facilitates efficient implementation. Numerical experiments validate the theoretical properties and demonstrate robust adaptive behavior for function-induced meshes and Rayleigh-Taylor instability simulations.

The remainder of this paper is organized as follows. Section 2 reviews equidistribution and alignment principles and proposes the new functional. Section 3 establishes its theoretical properties. Section 4 presents the geometric discretization and moving mesh algorithm. Finally, Section 5 reports numerical experiments demonstrating the method’s effectiveness.

2 Equidistribution and Alignment Conditions and Functional Construction

Adaptive moving mesh methods aim to redistribute mesh points toward regions of large solution variation, governed by the geometric principles of equidistribution and alignment rooted in \mathbf{M} -uniform meshes [14]. While foundational to many variational formulations [10, 12, 20], existing functionals often entail strong nonlinearity or dependence on empirical parameters that hinder numerical efficiency.

This section reviews these principles and introduces a new functional that preserves essential geometric properties while offering a simpler structure and superior optimization behavior, thereby facilitating the subsequent geometric discretization.

2.1 Equidistribution and Alignment Conditions

Let $\Omega_p \subset \mathbb{R}^d, d > 1$, be a bounded polygonal or polyhedral physical domain. Let

$$\mathbf{M} = \mathbf{M}(\mathbf{x}),$$

be a symmetric uniformly positive definite metric tensor defined on Ω_p , satisfying

$$m_0 \mathbf{I} \leq \mathbf{M}(\mathbf{x}) \leq m_1 \mathbf{I}, \quad \forall \mathbf{x} \in \Omega_p \quad (1)$$

where m_0 and m_1 are positive constants and \mathbf{I} denotes the identity matrix.

Let $\Omega_c \subset \mathbb{R}^d, d > 1$, be the computational domain, which is also assumed to be a bounded polygonal or polyhedral region with coordinates ξ . We consider a continuous coordinate transformation

$$\mathbf{x} = \mathbf{x}(\xi) : \Omega_c \rightarrow \Omega_p, \quad \xi = \xi(\mathbf{x}) = \mathbf{x}^{-1}(\mathbf{x}).$$

Under this mapping, the Jacobian matrix is defined as

$$\mathbf{J} = \frac{\partial \mathbf{x}}{\partial \xi} \in \mathbb{R}^{d \times d}, \det(\mathbf{J}) > 0.$$

2.1.1 Continuous Equidistribution and Alignment Conditions

We first define the total metric volume of the physical domain as

$$\sigma := \int_{\Omega_p} \sqrt{\det(\mathbf{M}(\mathbf{x}))} d\mathbf{x} = \int_{\Omega_c} \sqrt{\det(\mathbf{M}(\mathbf{x}(\xi)))} \det(\mathbf{J}(\xi)) d\xi. \quad (2)$$

The integrand

$$\rho := \sqrt{\det(\mathbf{M}(\mathbf{x}))},$$

represents the metric density function. The equidistribution condition requires that the metric volume elements be uniformly distributed over the computational domain Ω_c , which leads to the constraint

$$\rho \det(\mathbf{J}) = \frac{\sigma}{|\Omega_c|}, \quad \text{in } \Omega_c, \quad (3)$$

where $|\Omega_c|$ denotes the volume of the computational domain.

Let $d\mathbf{x}$ and $d\xi$ denote line elements in the physical and computational domains, respectively, related by $d\mathbf{x} = \mathbf{J}d\xi$. The metric length element can then be expressed as

$$\|\mathbf{d}\mathbf{x}\|_M^2 = \mathbf{d}\mathbf{x}^T \mathbf{M} \mathbf{d}\mathbf{x} = \mathbf{d}\xi^T (\mathbf{J}^T \mathbf{M} \mathbf{J}) \mathbf{d}\xi.$$

Thus, the tensor $\mathbf{J}^T \mathbf{M} \mathbf{J}$ represents the pullback metric in the computational domain. The alignment condition requires this pullback metric to be proportional to the identity matrix, i.e.,

$$\mathbf{J}^T \mathbf{M} \mathbf{J} = \eta(\xi) \mathbf{I}, \quad \text{in } \Omega_c,$$

or equivalently,

$$\mathbf{J}^{-1} \mathbf{M}^{-1} \mathbf{J}^{-T} = \theta(\xi) \mathbf{I}, \quad (4)$$

where $\eta(\xi)$ and $\theta(\xi)$ are scalar scaling functions.

This condition can also be written in scalar form as

$$\frac{1}{d} \text{tr}(\mathbf{J}^{-1} \mathbf{M}^{-1} \mathbf{J}^{-T}) = (\det(\mathbf{J}^{-1} \mathbf{M}^{-1} \mathbf{J}^{-T}))^{1/d}. \quad (5)$$

To consistently enforce both equidistribution and alignment, the scaling factor $\theta(\xi)$ is further constrained by the equidistribution condition, yielding

$$\theta = \left(\frac{\sigma}{|\Omega_c|} \right)^{-2/d} \quad (6)$$

Consequently, the combined EA condition takes the form

$$\mathbf{J}^{-1} \mathbf{M}^{-1} \mathbf{J}^{-T} = \left(\frac{\sigma}{|\Omega_c|} \right)^{-2/d} \mathbf{I}. \quad (7)$$

Several equivalent variants of this condition can be found in the literature; see, for example, [14].

2.1.2 Element-wise Mesh Discretization

We introduce a physical mesh $\mathcal{T}_p(K)$ and a computational mesh $\mathcal{T}_c(K)$ over the two domains, respectively.

Each element, denoted by $K_p \in \mathcal{T}_p(K)$ and $K_c \in \mathcal{T}_c(K)$, is a simplex, and K_p is the image of K_c under the physical mapping.

As illustrated in Figure 1, the continuous mapping $\mathbf{x}(\xi)$ is approximated on each element by an affine transformation:

$$\mathbf{x}(\xi)|_{K_c} \approx \mathbf{J}_K \xi + \mathbf{b}_K,$$

where \mathbf{J}_K is the Jacobian matrix associated with the affine mapping on the simplex K_c .

Based on this element-wise affine approximation, the equidistribution and alignment conditions can be naturally transferred to the discrete, element level.

Discrete equidistribution condition

$$\rho_K \det(\mathbf{J}_K) = \frac{\sigma_h}{|\Omega_c|}, \quad \forall K \quad (8)$$

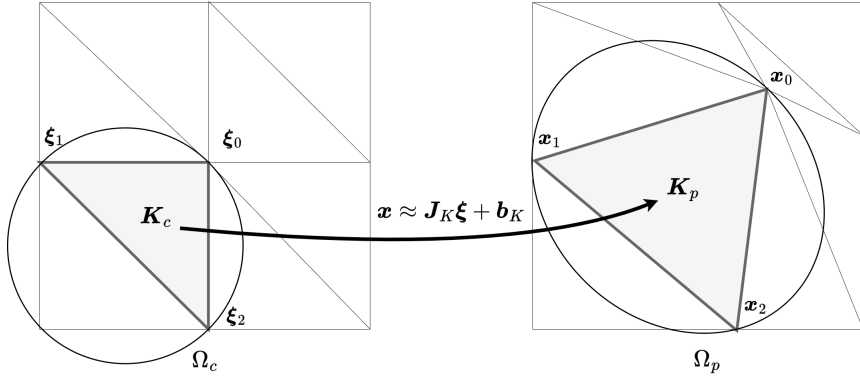


Figure 1: Element-wise affine approximation.

where

$$\sigma_h = \sum_{K \in \mathcal{T}_c} |K| \rho_K, \quad \rho_K = \sqrt{\det(\mathbf{M}_K)},$$

with \mathbf{M}_K being the average of $\mathbf{M}(\mathbf{x})$ over the element K_p .

Discrete alignment condition

$$\mathbf{J}_K^{-1} \mathbf{M}_K^{-1} \mathbf{J}_K^{-T} = \theta_K \mathbf{I} \quad , \forall K \quad (9)$$

or equivalently,

$$\frac{1}{d} \text{tr}(\mathbf{J}_K^{-1} \mathbf{M}_K^{-1} \mathbf{J}_K^{-T}) = (\det(\mathbf{J}_K^{-1} \mathbf{M}_K^{-1} \mathbf{J}_K^{-T}))^{1/d} \quad , \forall K \quad (10)$$

By combining the discrete equidistribution and alignment conditions, we obtain the following element-wise combined condition.

Discrete combined condition

$$\mathbf{J}_K^{-1} \mathbf{M}_K^{-1} \mathbf{J}_K^{-T} = \left(\frac{\sigma_h}{|\Omega_c|} \right)^{-2/d} \mathbf{I}. \quad (11)$$

2.2 Basic Functional Structure and Existing Functionals

In general, we consider mesh functionals of the following form:

$$I[\xi] = \int_{\Omega_p} G(\mathbf{J}^{-1}, \det(\mathbf{J}^{-1}), \mathbf{M}, \mathbf{x}) d\mathbf{x},$$

where G is a given smooth function.

We now review two representative mesh functionals from the literature. The first example is the equidistribution-alignment (EA) functional proposed by Huang [10]:

Example 2.1 (Huang's functional).

$$I[\xi] = \mu \int_{\Omega} \rho \left(\text{tr}(\mathbf{J}^{-1} \mathbf{M}^{-1} \mathbf{J}^{-T}) \right)^{\frac{d\gamma}{2}} d\mathbf{x} + (1 - 2\mu) d^{\frac{d\gamma}{2}} \int_{\Omega} \frac{\rho}{(\det(\mathbf{J})\rho)^\gamma} d\mathbf{x} \quad (12)$$

Here $\text{tr}(\cdot)$ denotes the matrix trace, $\mu \in [0, 1]$, and $\gamma > 0$.

This functional is constructed as a linear combination of the equidistribution and alignment conditions. It is coercive, polyconvex, and admits a minimizer; see [14] for its derivation and theoretical properties. The functional has been successfully applied in various settings, and its nonlinearity is relatively moderate, although it involves the empirical parameter μ .

The second example is an EA functional based on the Frobenius norm [20]:

Example 2.2 (Kolasinski-Huang functional).

$$I[\xi] = \int_{\Omega} \rho \|\mathbf{J}^{-1} \mathbf{M}^{-1} \mathbf{J}^{-T} - \left(\frac{\sigma}{|\Omega|_c} \right)^{-\frac{2}{d}} \mathbf{I}\|_F^{2\gamma} d\mathbf{x}. \quad (13)$$

Here $\|\cdot\|_F$ denotes the Frobenius norm.

This functional can be directly derived from the combined EA condition eq. (11). It avoids the empirical parameter μ appearing in functional eq. (12) and is likewise coercive and polyconvex. However, it is sensitive to the choice of γ , and its nonlinearity increases rapidly as γ becomes large.

The above functionals share a common structural form. Motivated by this observation, we introduce the following notation:

$$\mathbf{A} = \mathbf{J}^{-1} \mathbf{M}^{-1} \mathbf{J}^{-T}, \quad \alpha = \det \mathbf{A}. \quad (14)$$

Here, \mathbf{A} represents the pullback of the dual metric \mathbf{M}^{-1} .

With this change of variables, the mesh functional can be rewritten as

$$I[\xi] = \int_{\Omega_p} G(\mathbf{A}, \alpha, \mathbf{M}, \mathbf{x}) d\mathbf{x}. \quad (15)$$

For instance, functional eq. (12) can be expressed as

$$I[\xi] = \int_{\Omega_p} \mu \rho (\text{tr}(\mathbf{A}))^{\frac{d\gamma}{2}} + (1 - 2\mu) d^{\frac{d\gamma}{2}} \rho \alpha^{\frac{\gamma}{2}} d\mathbf{x}, \quad (16)$$

while functional eq. (13) becomes

$$I[\xi] = \int_{\Omega_p} \rho \|\mathbf{A} - \theta \mathbf{I}\|_F^{2\gamma} d\mathbf{x}, \quad (17)$$

where $\theta = \left(\frac{\sigma}{|\Omega_c|}\right)^{-2/d}$.

This \mathbf{A} -based representation not only leads to a more compact formulation, but also facilitates the derivation and simplification of the discrete structure, which will be discussed in detail in Section 4.

2.3 Derivation of a New Functional

Before deriving the new functional, we recall two basic lemmas [19].

Lemma 2.1. *For a symmetric matrix \mathbf{S} , its determinant equals the product of its eigenvalues, and its trace equals the sum of its eigenvalues.*

Lemma 2.2. *If all eigenvalues of a symmetric matrix \mathbf{S} are equal, then \mathbf{S} is a constant multiple of the identity matrix.*

We consider the following basic functional defined on \mathbf{A} :

$$\mathcal{K}(\mathbf{A}) = \text{tr}(\mathbf{A}) - \theta \ln \det(\mathbf{A}).$$

Due to the symmetry of \mathbf{A} and Lemma 2.1, let $\lambda_i, i = 1, \dots, d$, denote the eigenvalues of \mathbf{A} .

Then

$$\text{tr}(\mathbf{A}) = \sum_i^d \lambda_i, \quad \det(\mathbf{A}) = \prod_i^d \lambda_i.$$

Applying the arithmetic-geometric mean inequality yields

$$\begin{aligned} \mathcal{K}(\mathbf{A}) &\geq \text{tr}(\mathbf{A}) - \theta \ln \left(\frac{1}{d} \text{tr}(\mathbf{A}) \right)^d \\ &= d \left(\frac{1}{d} \text{tr}(\mathbf{A}) - \theta \ln \left(\frac{1}{d} \text{tr}(\mathbf{A}) \right) \right) \\ &= d \left(\frac{1}{d} \sum_i^d \lambda_i - \theta \ln \left(\frac{1}{d} \sum_i^d \lambda_i \right) \right). \end{aligned}$$

The above expression attains its minimum when $\lambda_i = \theta$ for all i . By Lemma 2.2, the minimizer satisfies the alignment condition $\mathbf{A} = \theta \mathbf{I}$.

Motivated by this observation, we extend the functional to the following form:

$$G(\mathbf{A}, \alpha, \mathbf{M}) = \rho \left(\text{tr}(\mathbf{A})^{\frac{d\gamma}{2}} - d^{\frac{d\gamma}{2}} \frac{\gamma}{2} \theta^{\frac{d\gamma}{2}} \ln \alpha \right) = \rho T(\mathbf{A}, \alpha), \quad (18)$$

where $T(\mathbf{A}, \alpha) = \text{tr}(\mathbf{A})^{\frac{d\gamma}{2}} - d^{\frac{d\gamma}{2}} \frac{\gamma}{2} \theta^{\frac{d\gamma}{2}} \ln \alpha$.

Recalling the definitions of \mathbf{A} and α in eq. (14), together with the combined EA condition eq. (11). This leads to the following new mesh energy functional:

$$I[\boldsymbol{\xi}] = \int_{\Omega_p} \rho \left(\text{tr}(\mathbf{A})^{\frac{d\gamma}{2}} - d^{\frac{d\gamma}{2}} \frac{\gamma}{2} \theta^{\frac{d\gamma}{2}} \ln \alpha \right) dx, \quad (19)$$

where $\theta = \left(\frac{\sigma}{|\Omega_c|} \right)^{-2/d}$, $\rho = \sqrt{\det(\mathbf{M})}$ and $\gamma > 1$.

This functional inherits the parameter-free property of the functional in eq. (13), while retaining the moderate nonlinearity characteristic of the functional in eq. (12). In the next section, we will show that it satisfies favorable convexity properties, making it suitable for the framework of variational adaptive mesh methods.

3 Properties of the Proposed Functional

This section establishes the fundamental theoretical properties of the proposed variational moving mesh functional, which are crucial for ensuring the well-posedness and robustness of the associated moving mesh algorithm. We begin by proving the scale invariance of the minimizer with respect to the metric tensor, a property essential for the practical implementation. Subsequently, we demonstrate the polyconvexity and geodesical convexity of the functional—key ingredients that facilitate the analysis of coercivity and the existence of minimizers. Building upon these results and leveraging established MMPDE theory, we further prove the non-degeneracy (non-singularity) of the mesh trajectory and the existence of a limiting mesh generated by the functional.

3.1 Scale Invariance

Theorem 3.1 (Scale Invariance of the Minimizer). *Let $\tilde{\mathbf{M}} = c\mathbf{M}$ for a constant $c > 0$. Then the proposed functional I satisfies*

$$I[\boldsymbol{\xi}; \tilde{\mathbf{M}}] = a(c, \mathbf{M}) \cdot I[\boldsymbol{\xi}; \mathbf{M}] + b(c, \mathbf{M}),$$

where $a(c, \mathbf{M}) > 0$ and $b(c, \mathbf{M})$ are functions that depend solely on c and \mathbf{M} (and are independent of the mapping $\boldsymbol{\xi}$). Consequently, the minimizer is invariant under uniform scaling of the metric tensor, i.e.,

$$\arg \min_{\boldsymbol{\xi}} I[\boldsymbol{\xi}, \tilde{\mathbf{M}}] = \arg \min_{\boldsymbol{\xi}} I[\boldsymbol{\xi}, \mathbf{M}].$$

Proof. From the definition of the functional in eq. (19), a direct calculation yields

$$I[\boldsymbol{\xi}, \tilde{\mathbf{M}}] = c^{\frac{d}{2} - \frac{d\gamma}{2}} I[\boldsymbol{\xi}, \mathbf{M}] + c^{\frac{d}{2} - \frac{d\gamma}{2}} \rho g(c, \mathbf{M}),$$

where $g(c, \mathbf{M}) = d^{\frac{d\gamma}{2}} \theta^{\frac{d\gamma}{2}} \ln c$. Hence, defining

$$a(c, \mathbf{M}) = c^{\frac{d}{2} - \frac{d\gamma}{2}}, \quad b(c, \mathbf{M}) = c^{\frac{d}{2} - \frac{d\gamma}{2}} \rho g(c, \mathbf{M}),$$

Observe that $a(c, \mathbf{M}) > 0$ and both a and b are independent of $\boldsymbol{\xi}$. \square

Remark 3.1. *Scale invariance indicates that global metric scaling does not affect the final mesh distribution. In practice, metrics are often normalized as $\tilde{\mathbf{M}} \geq \mathbf{I}$; a stretching factor $\kappa = (d^{\frac{d\gamma}{2}} \theta^{\frac{d\gamma}{2}} (1 - \frac{d\gamma}{2} \ln \theta))^{-1}$ may be applied to improve numerical conditioning.*

3.2 Convexity-Related Properties

To analyze the existence and regularity of minimizers, we employ the framework of polyconvexity in the sense of Ball [3]. We view the functional as depending on the inverse Jacobian $\mathbf{P} = \mathbf{J}^{-1}$. Recall that a function is called polyconvex if it can be expressed as a convex function of \mathbf{P} , its cofactor matrix $\text{Cof}(\mathbf{P})$, and its determinant $\det(\mathbf{P})$.

Theorem 3.2 (Polyconvexity). *The functional eq. (19) is polyconvex with respect to \mathbf{J}^{-1} . More precisely, consider I as a function of \mathbf{P} and $r = \det(\mathbf{P})$. Then, for any arbitrary variations $\Xi = (\xi_{ij})$ in \mathbf{P} and η in r , the following second-variation inequality holds:*

$$\frac{\partial^2 I}{\partial P_{ij} \partial P_{kl}} \xi_{ij} \xi_{kl} + \frac{\partial^2 I}{\partial r^2} \eta^2 \geq 0.$$

Proof. The weight function ρ is positive and independent of \mathbf{P} ; therefore, it scales the second variation uniformly and does not affect its sign. Hence, for the purpose of proving polyconvexity, it suffices to consider the core part $T(\mathbf{A}, \alpha)$ defined in eq. (18), where $\mathbf{A} = \mathbf{P}\mathbf{M}^{-1}\mathbf{P}^T$ and $\alpha = \det(\mathbf{A})$. We compute the first and second variations of I with respect to \mathbf{P} . Let $\Xi = (\xi_{ij})$ be an arbitrary variation of \mathbf{P} . The corresponding first variation of \mathbf{A} is

$$\mathbf{B} := \frac{\partial A_{\alpha\beta}}{\partial P_{ij}} \xi_{ij} = \Xi^T \mathbf{M}^{-1} \mathbf{P} + \mathbf{P}^T \mathbf{M}^{-1} \Xi,$$

which is a symmetric matrix. then we have:

$$\frac{\partial I}{\partial P_{ij}} \xi_{ij} = \frac{\partial I}{\partial A_{\alpha\beta}} \frac{\partial A_{\alpha\beta}}{\partial P_{ij}} \xi_{ij} = \frac{d\gamma}{2} \text{tr}(\mathbf{A})^{\frac{d\gamma}{2}-1} \text{tr}(\mathbf{B}),$$

Furthermore

$$\frac{\partial^2 I}{\partial P_{ij} \partial P_{kl}} \xi_{ij} \xi_{kl} = \frac{d\gamma}{2} \left(\frac{d\gamma}{2} - 1 \right) \text{tr}(\mathbf{A})^{\frac{d\gamma}{2}-2} \text{tr}(\mathbf{B})^2 + d\gamma \text{tr}(\mathbf{A})^{\frac{d\gamma}{2}-1} \text{tr}(\mathbf{C}),$$

where $\mathbf{C} := 2\Xi^T \mathbf{M}^{-1} \Xi$. We also have

$$\frac{\partial I}{\partial r} = -d^{\frac{d\gamma}{2}} \frac{\gamma}{2} \theta^{\frac{d\gamma}{2}} \frac{1}{g} 2r\rho^2 = -2d^{\frac{d\gamma}{2}} \frac{\gamma}{2} \theta^{\frac{d\gamma}{2}} \frac{1}{r}.$$

Therefore,

$$\frac{\partial^2 I}{\partial r^2} \eta^2 = 2d^{\frac{d\gamma}{2}} \frac{\gamma}{2} \theta^{\frac{d\gamma}{2}} \frac{\eta^2}{r^2}.$$

Since \mathbf{M} is uniformly positive definite (by assumption eq. (1)), and \mathbf{J} is invertible, $\mathbf{A} = \mathbf{P}\mathbf{M}^{-1}\mathbf{P}^T$ inherits positive definiteness. Moreover, \mathbf{C} is a Gram matrix, hence positive semi-definite. Therefore

$$\frac{\partial^2 I}{\partial P_{ij} \partial P_{kl}} \xi_{ij} \xi_{kl} \geq 0, \quad \frac{\partial^2 I}{\partial r^2} \eta^2 \geq 0.$$

Since both quadratic forms are individually non-negative, their sum is also non-negative, which establishes the polyconvexity inequality. This means that the Hessian matrix is non-negative definite in all directions. By Ball's theorem, this confirms the polyconvexity of I with respect to \mathbf{P} . \square

Theorem 3.3 (Geodesical Convexity). *The functional I defined in eq. (19) is geodesically convex with respect to the variable $\mathbf{P} = \mathbf{J}^{-1}$ on the manifold of invertible matrices. Specifically, for any two points \mathbf{P}_1 and \mathbf{P}_2 , the functional satisfies the following subgradient inequality along the natural geodesic connecting them:*

$$I(\mathbf{P}_1) - I(\mathbf{P}_2) \geq \left\langle \frac{\partial I}{\partial \mathbf{P}} \Big|_{\mathbf{P}=\mathbf{P}_2}, \eta(\mathbf{P}_1, \mathbf{P}_2) \right\rangle,$$

where $\eta(\mathbf{P}_1, \mathbf{P}_2)$ is a tangent vector at \mathbf{P}_2 that points towards \mathbf{P}_1 . This property implies that every critical point of I is a global minimizer, which is crucial for the convergence of gradient-based optimization algorithms.

Proof. Since the functional I is a sum of two terms, and the desired inequality is preserved under addition, it suffices to prove the inequality for each term separately.

For $\text{tr}(\mathbf{A})^{\frac{d\gamma}{2}}$, which is convex with respect to \mathbf{A} , atisfies a standard subgradient inequality in \mathbf{A} -space, which, after pulling back to \mathbf{P} -space via the chain rule, yields an inequality of the form theorem 3.2.

For the term

$$\bar{I}(\mathbf{A}) := -C \ln \det(\mathbf{A}),$$

where $C = d^{\frac{d\gamma}{2}} \frac{\gamma}{2} \theta^{\frac{d\gamma}{2}}$, we invoke the geodesic convexity of $-\ln \det(\cdot)$ on the manifold of symmetric positive definite matrices. A direct calculation shows that for any $\mathbf{A}_1, \mathbf{A}_2 \succ 0$,

$$\bar{I}(\mathbf{A}_1) - \bar{I}(\mathbf{A}_2) = -C \ln \frac{\det(\mathbf{A}_1)}{\det(\mathbf{A}_2)}.$$

Meanwhile, taking the particular direction $\bar{\eta} = \mathbf{A}_1$ at \mathbf{A}_2 . We have

$$\left\langle \frac{\partial \bar{I}}{\partial \mathbf{A}_2}, \bar{\eta} \right\rangle = -C \text{tr}(\mathbf{A}_2^{-1} \mathbf{A}_1).$$

Using the arithmetic-geometric mean inequality $\text{tr} \mathbf{X} \geq d \det(\mathbf{X})^{1/d}$ for any $\mathbf{X} \succ 0$, we obtain

$$\begin{aligned} \left\langle \frac{\partial \bar{I}}{\partial \mathbf{A}_2}, \bar{\eta} \right\rangle &\leq -Cd \det(\mathbf{A}_2^{-1} \mathbf{A}_1)^{\frac{1}{d}} \\ &\leq -C \ln \det(\mathbf{A}_2^{-1} \mathbf{A}_1) = \bar{I}(\mathbf{A}_1) - \bar{I}(\mathbf{A}_2). \end{aligned}$$

By the geodesic convexity of $-\ln \det(\cdot)$ on the manifold of symmetric positive definite matrices, for any $\mathbf{A}_1, \mathbf{A}_2 \succ 0$ there exists a tangent direction $\tilde{\eta}(\mathbf{A}_1, \mathbf{A}_2)$ at \mathbf{A}_2 such that the subgradient inequality

$$I(\mathbf{A}_1) - I(\mathbf{A}_2) \geq \left\langle \frac{\partial I}{\partial \mathbf{A}_2}, \tilde{\eta}(\mathbf{A}_1, \mathbf{A}_2) \right\rangle,$$

holds. A concrete choice is the Riemannian logarithm $\tilde{\eta}(\mathbf{A}_1, \mathbf{A}_2) = \log_{\mathbf{A}_2}(\mathbf{A}_1) = \mathbf{A}_2^{1/2} \log(\mathbf{A}_2^{-1/2} \mathbf{A}_1 \mathbf{A}_2^{-1/2}) \mathbf{A}_2^{1/2}$, which reduces to the Euclidean direction $\mathbf{A}_1 - \mathbf{A}_2$ when the affine-invariant metric is replaced by the Euclidean metric. Both choices satisfy the above inequality and therefore certify the claimed existence of such a tangent vector.

We now pull it back to the \mathbf{P} -variable. Since $\mathbf{A} = \mathbf{P} \mathbf{M}^{-1} \mathbf{P}^T$, applying the chain rule yields the desired inequality for \mathbf{P} :

$$\begin{aligned} I(\mathbf{P}_1) - I(\mathbf{P}_2) &\geq \left\langle \frac{\partial I}{\partial \mathbf{A}_2}, \tilde{\eta}(\mathbf{A}_1, \mathbf{A}_2) \right\rangle \\ &= \left\langle \frac{\partial I}{\partial (P_2)_{ij}} \frac{\partial (P_2)_{ij}}{\partial (A_2)_{kl}}, (\tilde{\eta}(\mathbf{A}_1, \mathbf{A}_2))_{kl} \right\rangle \\ &= \left\langle \frac{\partial I}{\partial (P_2)_{ij}}, \frac{\partial (P_2)_{ij}}{\partial (A_2)_{kl}} (\tilde{\eta}(\mathbf{A}_1, \mathbf{A}_2))_{kl} \right\rangle. \end{aligned}$$

Applying the chain rule with the right-inverse choice $\delta \mathbf{P} = \frac{1}{2} \delta \mathbf{A} \mathbf{P}^{-T} \mathbf{M}$, we obtain

$$\frac{\partial (P_2)_{ij}}{\partial (A_2)_{kl}} = \frac{1}{2} (\mathbf{P}_2^{-T} \mathbf{M})_{j\ell} \delta_{ik}, \quad \text{hence} \quad (\eta(\mathbf{P}_1, \mathbf{P}_2))_{ij} = \frac{1}{2} (\tilde{\eta}(\mathbf{A}_1, \mathbf{A}_2) \mathbf{P}_2^{-T} \mathbf{M})_{ij}.$$

Substituting this into the chain-rule expression yields

$$I(\mathbf{P}_1) - I(\mathbf{P}_2) \geq \left\langle \frac{\partial I}{\partial \mathbf{P}_2}, \eta(\mathbf{P}_1, \mathbf{P}_2) \right\rangle,$$

which completes the pullback to the \mathbf{P} -variable. This completes the proof of geodesic convexity. \square

3.3 Coercivity and Existence of Minimum

Theorem 3.4 (Coercivity). *The functional eq. (19) is enforced when $\gamma > 1$, that is, there exist $\alpha > 0, \beta \geq 0$ as constants such that*

$$G \geq \alpha \text{tr}(\mathbf{A})^{\frac{d\gamma}{2}} - \beta.$$

Proof. Since

$$I[\boldsymbol{\xi}] = \int_{\Omega_p} G(\mathbf{A}, \alpha, \mathbf{M}) d\mathbf{x} = \int_{\Omega_p} \rho T(\mathbf{A}, \alpha) d\mathbf{x}$$

and

$$\begin{aligned} T(\mathbf{A}, \alpha) &= \text{tr}(\mathbf{A})^{\frac{d\gamma}{2}} - d^{\frac{d\gamma}{2}} \frac{\gamma}{2} \theta^{\frac{d\gamma}{2}} \ln \det(\mathbf{A}) \\ &\geq \text{tr}(\mathbf{A})^{\frac{d\gamma}{2}} - d^{\frac{d\gamma}{2}} \frac{\gamma}{2} \theta^{\frac{d\gamma}{2}} \ln \left(\frac{1}{d} \text{tr}(\mathbf{A}) \right)^d \\ &= d^{\frac{d\gamma}{2}} \left(\left(\frac{\sum_i^d \lambda_i}{d} \right)^{\frac{d\gamma}{2}} - \theta^{\frac{d\gamma}{2}} \ln \left(\frac{\sum_i^d \lambda_i}{d} \right)^{\frac{d\gamma}{2}} \right). \end{aligned}$$

The equality holds if and only if $\mathbf{A} = \theta \mathbf{I}$. For the above structure, using the elementary inequality

$$x - a \ln x \geq cx + a \left(1 + \ln \frac{a}{1-c} \right), \quad a > 0, \quad c \in (0, 1),$$

with $x = \left(\frac{\sum_i^d \lambda_i}{d}\right)^{\frac{d\gamma}{2}}$ and $a = \theta^{\frac{d\gamma}{2}}$, we obtain for any $c \in (0, 1)$:

$$\begin{aligned} T(\mathbf{A}, \alpha) &\geq d^{\frac{d\gamma}{2}} c \left(\frac{\sum_i^d \lambda_i}{d}\right)^{\frac{d\gamma}{2}} + d^{\frac{d\gamma}{2}} \theta^{\frac{d\gamma}{2}} \left(1 + \ln \frac{\theta^{\frac{d\gamma}{2}}}{1-c}\right) \\ &= \text{ctr}(\mathbf{A})^{\frac{d\gamma}{2}} - C(c, \theta), \end{aligned}$$

where $C(c, \theta) = -d^{\frac{d\gamma}{2}} \theta^{\frac{d\gamma}{2}} \left(1 + \ln \frac{\theta^{\frac{d\gamma}{2}}}{1-c}\right)$. Choosing $c_0 \in [1 - \varepsilon, 1)$ with $\varepsilon = \min\{1, e\theta^{\frac{d\gamma}{2}}\}$ such that $C(c_0, \theta) \geq 0$, we get

$$G(\mathbf{A}, \alpha, \mathbf{M}) \geq c_0 \rho_0 \text{tr}(\mathbf{A})^{\frac{d\gamma}{2}} - \rho_1 C(c_0, \theta),$$

where $\rho_0 = m_0^{d/2}$, $\rho_1 = m_1^{d/2}$. Let $\alpha = c_0 \rho_0$ and $\beta = \rho_1 C(c_0, \theta)$. \square

Theorem 3.5. *The functional $I(\xi)$ defined in eq. (19) admits at least one minimizer.*

Proof. According to Theorem 3.2, the functional $I(\xi)$ is polyconvex with respect to the geometric variables. Moreover, Theorem 3.5 shows that $I(\xi)$ is coercive, i.e., its value tends to infinity as the mesh elements degenerate or their sizes become unbounded. These two properties ensure that all the assumptions of the existence theorem for polyconvex mesh functionals established by Huang (see Theorem 6.2.2 in [14]) are satisfied. Therefore, the functional eq. (19) admits at least one minimizer over the admissible set of meshes. \square

Remark 3.2. *The geodesic convexity (theorem 3.3) combined with the existence of a minimizer ensures that every critical point of I is a global minimizer. This fundamental property guarantees that any gradient-based optimization algorithm converges to a globally optimal mesh configuration, eliminating the risks of local minima or saddle point entrapment. This strong theoretical foundation is crucial for the practical reliability of the moving mesh algorithm and differentiates our approach from functionals lacking such convexity guarantees.*

3.4 Mesh nonsingularity and the existence of limit meshes

If the descent of the mesh functional is considered as a gradient flow process, then we have:

$$\frac{d\xi_i}{dt} = -\frac{P_i}{\tau} \left(\frac{\partial I_h}{\partial \xi_i}\right)^T \quad \text{or} \quad \frac{d\mathbf{x}_i}{dt} = -\frac{P_i}{\tau} \left(\frac{\partial I_h}{\partial \mathbf{x}_i}\right)^T, \quad i = 1, \dots, d. \quad (20)$$

The gradient flow equations described above form the core structure of the MMPDE method, where P_i is the balance function, and τ is the time-scale parameter. For $t > 0$ and with a non-singular initial mesh, the gradient flow equations generate a time-dependent mesh sequence $\mathcal{T}_t(\square)$. We denote the minimum height of a element K measured in the metric \mathbf{M}_K as $a_{K, \mathbf{M}}$.

Corollary 3.6. *For any $t > 0$, when $\gamma > 1$, the mesh semi-discrete PDE eq. (20) generated by the functional eq. (19) enjoys the following properties: if all elements in the mesh trajectory have positive volume at the initial time, then they preserve positive volume for all $t > 0$. Moreover, the minimum height measured in the metric \mathbf{M} and the element volume admit the following uniform lower bounds:*

$$a_{K, \mathbf{M}} \geq C_1 r_0^{\frac{\gamma}{\gamma-1}} m_1^{-\frac{1}{2(\gamma-1)}} N C^{-\frac{\gamma}{d\gamma-d}} \quad \forall K \in \mathcal{T}_t, \forall t > 0, \quad (21)$$

$$|K| \geq C_2 r_0^{\frac{d\gamma}{\gamma-1}} m_1^{-\frac{d}{2(\gamma-1)} - \frac{d}{2}} N C^{-\frac{\gamma}{\gamma-1}} \quad \forall K \in \mathcal{T}_t, \forall t > 0. \quad (22)$$

Here $r_0 N^{-1/d} \leq r_{K_c}$ and $R_{K_c} \leq r_1 N C^{-1/d}$, where m_0 and m_1 are defind in (1), and R_{K_c} and r_{K_c} denote the maximum diameters of the circumscribed and inscribed ellipses of an element, respectively. The constants in the above estimates are given by

$$C_1 = \left(\frac{\alpha \hat{a}^{4\gamma}}{d! \hat{h}^{4\gamma} (\beta |\Omega_p| + I_h(\mathcal{T}_p(0)))} \right)^{\frac{1}{4\gamma-d}}, \quad C_2 = \frac{C_1^d}{d!},$$

where \hat{h} and \hat{a} are the diameter and height of the reference simplex \hat{K} , α and β be the coercivity constants given in Theorem 3.5, $|\Omega_p|$ be the volume of the physical domain, and $I_h(\mathcal{T}_p(0))$ denotes the value of the discrete functional evaluated on the initial mesh.

Proof. Recall from (1) that $m_0 \mathbf{I} \leq \mathbf{M}(\mathbf{x}) \leq m_1 \mathbf{I}$. Define $\rho_0 = m_0^{d/2}$ and $\rho_1 = m_1^{d/2}$, and let r_0, r_1 denote bounds on the reference element geometry. By Theorem 3.5 (coercivity), we have

$$G(\mathbf{A}, \alpha, \mathbf{M}) \geq \alpha \text{tr}(\mathbf{A})^{\frac{d\gamma}{2}} - \beta$$

with α, β as defined therein. Applying Huang's Theorem 6.3.2 (see [14]) with $q = \frac{d\gamma}{2}$ yields the bounds eq. (21)-eq. (22). \square

Based on the mesh nonsingularity established in Corollary 3.1 and the existence theory for limiting meshes [13], the mesh trajectory generated by the gradient flow eq. (20) of our functional possesses the following properties for any non-singular initial mesh:

1. The discrete energy functional converges as time tends to infinity:

$$\lim_{t \rightarrow \infty} I_h(\mathcal{T}_h(t)) = L.$$

2. The mesh trajectory admits at least one limiting mesh. All such limiting meshes are non-singular and satisfy the lower bound estimates for element heights and volumes given by eq. (21) and eq. (22). 3. Every limiting mesh is a critical point of the discrete functional I_h , i.e., it satisfies the equilibrium condition

$$\frac{\partial I_h}{\partial \mathbf{x}_i} = \mathbf{0} \quad \text{for all nodes } i.$$

These properties guarantee the long-time stability and well-posedness of the mesh adaptation process driven by the proposed functional.

4 Geometric Discretization for Functionals and Moving Mesh Algorithms

In this section, we present the geometric discretization of the proposed functional and the corresponding moving mesh algorithm.

Our discrete framework is based on the geometric discretization methodology developed by Huang [12], which has several notable advantages: it preserves essential geometric properties, guarantees mesh nonsingularity, admits explicit discrete expressions, and is straightforward to implement in practice.

To obtain more compact discrete and gradient expressions, we introduce the pullback tensor \mathbf{A} into the functional and adopt a unified element-level construction: both the discretization and the two assembly views (computational and physical coordinates) rely on the same set of local quantities per element. No separate local constructs are needed for the two views. This yields a more transparent derivation, a simpler assembly procedure, and a clearer variational interpretation, while allowing all expressions to be assembled consistently and efficiently. The unified perspective also facilitates practical implementation of the moving mesh algorithm, since the same local quantities are reused throughout discretization and optimization.

We adopt two complementary perspectives for the discretization: the computational coordinate (ξ -view), and the physical coordinate (\mathbf{x} -view). Both viewpoints give rise to gradient flow systems associated with the discrete energy functional, and the relationship between them is clarified through the use of the tensor \mathbf{A} .

4.1 Discrete Energy Functional and Gradient Flow

After mesh discretization, the functional eq. (19) can be written as

$$\begin{aligned} I_h &= \sum_{K \in \mathcal{T}_h} |K| G(\mathbf{A}_K, \alpha_K, \mathbf{M}_K) \\ &= \sum_{K \in \mathcal{T}_h} |K| \rho_K T(\mathbf{A}_K, \alpha_K), \end{aligned} \tag{23}$$

where

$$\mathbf{A}_K = \mathbf{J}_K^{-1} \mathbf{M}_K^{-1} \mathbf{J}_K^{-1}, \quad \alpha_K = \det(\mathbf{A}_K).$$

Here, \mathbf{J}_K denotes the Jacobian matrix of element K , and the metric tensor \mathbf{M}_K is obtained by averaging its values at the element vertices. Discretizing the energy functional I_h naturally introduces a gradient flow structure with respect to the computational coordinates $\{\xi_i\}$. Specifically, the evolution of the mesh in the ξ -view is governed by

$$\frac{\partial \xi_i}{\partial t} = -\frac{P_i}{\tau} \frac{\partial I_h}{\partial \xi_i}, \quad i = 0, \dots, NN-1 \tag{24}$$

where P_i is a balancing function and τ is a user-defined time-scale parameter. This discrete gradient flow serves as a semi-discrete correspondence to the continuous MMPDE and guarantees the monotonically decreasing discrete energy I_h . The global gradient, however, needs to be constructed from the local gradients of the cells by

$$\frac{\partial I_h}{\partial \xi_i} = \sum_{K \in S_i} |K| \frac{\partial I_K}{\partial [\xi_0^K, \xi_1^K, \dots, \xi_d^K]}, \quad i = 0, \dots, NN-1 \quad (25)$$

where S_i denotes the element star associated with node i . Alternatively, one may directly evolve the physical mesh points without explicitly tracking the mapping from computational to physical coordinates. This physical-coordinate formulation leads to the following system of ordinary differential equations:

$$\frac{\partial \mathbf{x}_i}{\partial t} = -\frac{P_i}{\tau} \frac{\partial I_h}{\partial \mathbf{x}_i}, \quad i = 0, \dots, NN-1 \quad (26)$$

The discrete gradient in the \mathbf{x} -view is assembled locally from element contributions as

$$\frac{\partial I_h}{\partial \mathbf{x}_i} = \sum_{K \in S_i} |K| \frac{\partial I_K}{\partial [\mathbf{x}_0^K, \mathbf{x}_1^K, \dots, \mathbf{x}_d^K]} = - \sum_{K \in S_i} |K| \mathbf{v}_j^K, \quad i = 0, \dots, NN-1 \quad (27)$$

where \mathbf{v}_j^K are the element-level velocities associated with the vertices of element K . In the following subsections, we derive and simplify the geometric discretizations associated with the element-level gradients in eq. (25) and eq. (27), highlighting how the use of the tensor \mathbf{A} leads to a more compact and efficient formulation, particularly for the physical-coordinate gradient flow.

4.2 Geometric Discretization of Gradient

Now, the vertex coordinates $\mathbf{x}_0^K, \dots, \mathbf{x}_d^K$ of cell K and the vertex coordinates ξ_0^K, \dots, ξ_d^K of \hat{K} satisfy the following relationship:

$$\mathbf{x}_i^K - \mathbf{x}_0^K = \mathbf{J}_K(\xi_i^K - \xi_0^K), \quad i = 1, \dots, d$$

We denote

$$E_K = [\mathbf{x}_1^K - \mathbf{x}_0^K, \dots, \mathbf{x}_d^K - \mathbf{x}_0^K], \quad \hat{E}_K = [\xi_1^K - \xi_0^K, \dots, \xi_d^K - \xi_0^K]$$

as the edge matrices of units K and \hat{K} respectively. Using $E_K, \hat{E}_K, \mathbf{J}_K$ and $r_K = \det \mathbf{J}_K$, the unit gradient expression of such functionals is given explicitly and without loss of generality:

$$\frac{\partial I_K}{\partial [\xi_1^K, \dots, \xi_d^K]} = E_K^{-1} \frac{\partial G}{\partial \mathbf{J}_K^{-T}} + \frac{\partial G}{\partial r_K} \frac{\det(\hat{E}_K)}{\det(E_K)} \hat{E}_K^{-1} \quad (28)$$

$$\frac{\partial I_K}{\partial \xi_0^K} = -\mathbf{e}^T \frac{\partial I_K}{\partial [\xi_1^K, \dots, \xi_d^K]}, \quad \mathbf{e} = [1, \dots, 1]^T \quad (29)$$

Discrete geometry based on a covariant perspective is expressed in [12] as:

$$\begin{bmatrix} (v_1^K)^T \\ \vdots \\ (v_d^K)^T \end{bmatrix} = -GE_K^{-1} + E_K^{-1} \frac{\partial G}{\partial \mathbf{J}_K^{-T}} \hat{E}_K E_K^{-1} + \frac{\partial G}{\partial r_K} \frac{\det(\hat{E}_K)}{\det(E_K)} E_K^{-1} - \frac{1}{d+1} \sum_{j=0}^d \text{tr} \left(\frac{\partial G}{\partial \mathbf{M}_K} \mathbf{M}_{j,K} \right) \begin{bmatrix} \frac{\partial \phi_{j,K}}{\partial \mathbf{x}} \\ \vdots \\ \frac{\partial \phi_{j,K}}{\partial \mathbf{x}} \end{bmatrix} - \frac{1}{d+1} \begin{bmatrix} \frac{\partial G}{\partial \mathbf{x}} \\ \vdots \\ \frac{\partial G}{\partial \mathbf{x}} \end{bmatrix}, \quad (30)$$

$$(v_0^K)^T = -\sum_{k=1}^d (v_k^K)^T - \sum_{j=0}^d \text{tr} \left(\frac{\partial G}{\partial \mathbf{M}_K} \mathbf{M}_{j,K} \right) \frac{\partial \phi_{j,K}}{\partial \mathbf{x}} - \frac{\partial G}{\partial \mathbf{x}}, \quad (31)$$

where $\mathbf{M}_{j,K} = \mathbf{M}(\mathbf{x}_j^K)$, $\phi_{j,K}$ are linear basis functions related to \mathbf{x}_j^K , and $\frac{\partial \phi_{j,K}}{\partial \mathbf{x}}$ are the physical gradients of $\phi_{j,K}$. This explicit expression is more complex than the contravariant perspective, and the metric \mathbf{M} also needs to be updated in this perspective.

These formulas ensure that the discrete gradient maintains the geometric invariance of the continuous functional, which guarantees the validity of our Corollary 3.6 and the nonsingularity conclusion given in Huang [13] in actual calculations. To our knowledge, this discretization expression is currently the only method proven to have the property of mesh nonsingularity.

Currently, this discrete structure has the advantages of explicit expression and ease of construction. We observe that this structure offers the potential for further simplification under the \mathbf{A} -structure functional, especially for the derivative of a specific functional with respect to the Jacobian and its determinant, which has a minimal form. On the other hand, our simplification can greatly facilitate the construction of discrete structures from a covariant perspective, and can avoid explicitly writing out the derivative of the functional with respect to \mathbf{M}_K , which is generally the most troublesome term.

4.3 Discrete Simplification of \mathbf{A} Structure

Before describing the discrete simplification scheme, we first give two fundamental lemmas:

Lemma 4.1. *For symmetric matrices \mathbf{G}, \mathbf{M} , the following equation holds:*

$$\text{tr}(\mathbf{G} \frac{\partial \mathbf{A} \mathbf{M} \mathbf{A}^T}{\partial \mathbf{A}^T}) = 2\mathbf{M} \mathbf{A}^T \mathbf{G}.$$

Lemma 4.2. *For any symmetric matrix \mathbf{G}, \mathbf{M} , the following equation holds:*

$$\text{tr}(\mathbf{G} \frac{\partial \mathbf{A} \mathbf{M}^{-1} \mathbf{A}^T}{\partial \mathbf{M}}) = -\mathbf{M}^{-1} \mathbf{A}^T \mathbf{G} \mathbf{A} \mathbf{M}^{-1}.$$

Proofs are given in Appendix B. Using Lemma 4.1, we have the following two expressions:

$$\frac{\partial G}{\partial \mathbf{J}_K^{-T}} = \rho_K \text{tr}(\frac{\partial T}{\partial \mathbf{A}_K} \frac{\partial \mathbf{A}_K}{\partial \mathbf{J}_K^{-T}}) = 2\rho_K \mathbf{M}_K^{-1} \mathbf{E}_K^{-T} \hat{\mathbf{E}}_K^T \frac{\partial T}{\partial \mathbf{A}_K} \quad (32)$$

$$\frac{\partial G}{\partial r_K} = \rho_K \frac{\partial T}{\partial \alpha_K} \frac{\partial \alpha_K}{\partial r_K} = 2\rho_K \det(\mathbf{M}_K)^{-1} \frac{\det(\hat{\mathbf{E}}_K)}{\det(\mathbf{E}_K)} \frac{\partial T}{\partial \alpha_K} \quad (33)$$

And let

$$\mathbf{R} := \begin{bmatrix} -1 & -1 & \cdots & -1 \\ 1 & 0 & \cdots & 0 \\ \vdots & \vdots & & \vdots \\ 0 & 0 & \cdots & 1 \end{bmatrix}_{(d+1) \times d}.$$

For eq. (28), we can rewrite it using eqs. (32) and (33) as:

$$\begin{aligned} \frac{\partial I_K}{\partial [\xi_1^K, \dots, \xi_d^K]} &= 2\rho_K (\mathbf{E}_K^{-1} \mathbf{M}_K^{-1} \mathbf{E}_K^{-T} \hat{\mathbf{E}}_K^T \frac{\partial T}{\partial \mathbf{A}_K} + \frac{\partial T}{\partial \alpha_K} \frac{1}{\det \mathbf{M}_K (\det \mathbf{J}_K)^2} \hat{\mathbf{E}}_K^{-1}) \\ &= 2\rho_K \hat{\mathbf{E}}_K^{-1} (\mathbf{A}_K \frac{\partial T}{\partial \mathbf{A}_K} + \alpha_K \frac{\partial T}{\partial \alpha_K} \mathbf{I}). \end{aligned}$$

We summarize the assembly process of the unit discrete gradient:

$$\frac{\partial I_K}{\partial [\xi_0^K, \xi_1^K, \dots, \xi_d^K]} = 2\rho_K \mathbf{R} \hat{\mathbf{E}}_K^{-1} (\mathbf{A}_K \frac{\partial T}{\partial \mathbf{A}_K} + \alpha_K \frac{\partial T}{\partial \alpha_K} \mathbf{I}). \quad (34)$$

Remark 4.1. *The above eq. (34) construction can be further transformed into a very standard affine structure, that is: let $\mathbf{Q}_K = \mathbf{A}_K \frac{\partial T}{\partial \mathbf{A}_K} + \alpha_K \frac{\partial T}{\partial \alpha_K} \mathbf{I}$, then, we rewrite it as*

$$\frac{\partial I_K}{\partial [\xi_0^K, \xi_1^K, \dots, \xi_d^K]} = 2\rho_K \mathbf{R} \hat{\mathbf{E}}_K^{-1} \mathbf{Q}_K \hat{\mathbf{E}}_K^{-T} \mathbf{R}^T [\xi_i^T] = \mathbf{W}_K [\xi_i^T],$$

where $\mathbf{W}_K = 2\rho_K \mathbf{R} \hat{\mathbf{E}}_K^{-1} \mathbf{Q}_K \hat{\mathbf{E}}_K^{-T} \mathbf{R}^T$.

Since it is easy to prove that for the structure $F(\text{tr}(\mathbf{A}_K), \|\mathbf{A}_K\|_F^2)$, the tensor derivatives of \mathbf{A}_K are all commutative with \mathbf{A}_K , \mathbf{W}_K is a symmetric matrix and is generally related to ξ_i . Taking the two-dimensional case as an example, we represent $\frac{\partial I_K}{\partial [\xi_0^K, \xi_1^K, \dots, \xi_d^K]}$ as the expanded structure of $\begin{bmatrix} \xi_i \\ \eta_i \end{bmatrix}$

$$\frac{\partial I_K}{\partial [\xi_i, \eta_i]^T} = \begin{bmatrix} \mathbf{W}_K & \mathbf{0} \\ \mathbf{0} & \mathbf{W}_K \end{bmatrix} \begin{bmatrix} \xi_i \\ \eta_i \end{bmatrix}.$$

For this structure, we can also use the standard unit-to-global mapping method to construct the global matrix, which can be well integrated into some mature code frameworks and helps us construct more possible step formats.

For the rewrites of eq. (30) and eq. (29), since the objects we consider here all satisfy $\frac{\partial G}{\partial \mathbf{x}} = \mathbf{0}$, we will ignore their last term.

$$\begin{bmatrix} (\frac{\partial \phi_{1,K}}{\partial \mathbf{x}})^T \\ \vdots \\ (\frac{\partial \phi_{d,K}}{\partial \mathbf{x}})^T \end{bmatrix} = E_K^{-1} \quad \text{and} \quad (\frac{\partial \phi_{0,K}}{\partial \mathbf{x}})^T = - \sum_{j=1}^d (\frac{\partial \phi_{j,K}}{\partial \mathbf{x}})^T.$$

We denote

$$\mathbf{V}_{d+1 \times d} := \begin{bmatrix} (\frac{\partial \phi_{0,K}}{\partial \mathbf{x}})^T \\ (\frac{\partial \phi_{1,K}}{\partial \mathbf{x}})^T \\ \vdots \\ (\frac{\partial \phi_{d,K}}{\partial \mathbf{x}})^T \end{bmatrix} = \mathbf{R} E_K^{-1}, \quad \mathbf{e} = \begin{bmatrix} 1 \\ \vdots \\ 1 \end{bmatrix}_{d+1}$$

Therefore, we can simplify the derivative term of \mathbf{M}_K as follows:

$$\begin{aligned} & \sum_{j=0}^d \text{tr} \left(\frac{\partial G}{\partial \mathbf{M}_K} \mathbf{M}_{j,K} \right) \begin{bmatrix} (\frac{\partial \phi_{j,K}}{\partial \mathbf{x}})^T \\ \vdots \\ (\frac{\partial \phi_{j,K}}{\partial \mathbf{x}})^T \end{bmatrix}_{d+1 \times d} \\ &= \begin{bmatrix} 1 \\ \vdots \\ 1 \end{bmatrix}_{d+1} \left[\text{tr} \left(\frac{\partial G}{\partial \mathbf{M}_K} \mathbf{M}_{0,K} \right) \dots \text{tr} \left(\frac{\partial G}{\partial \mathbf{M}_K} \mathbf{M}_{d,K} \right) \right] \begin{bmatrix} (\frac{\partial \phi_{0,K}}{\partial \mathbf{x}})^T \\ \vdots \\ (\frac{\partial \phi_{d,K}}{\partial \mathbf{x}})^T \end{bmatrix} = (\mathbf{e} \otimes \mathbf{u}) \mathbf{V}, \end{aligned}$$

where $i = 0, \dots, d-1, j, k = 0, \dots, d$, $\mathbf{u} = \text{tr} \left(\frac{\partial G}{\partial \mathbf{M}_K} \mathbf{M}_{j,K} \right)$. Drawing further upon the conclusions of eq. (32) and eq. (33), we have

$$\begin{aligned} \begin{bmatrix} (v_0^K)^T \\ (v_1^K)^T \\ \vdots \\ (v_d^K)^T \end{bmatrix} &= \rho_K \mathbf{R} \left(-T E_K^{-1} + 2 \hat{E}_K^{-1} \mathbf{A}_K \frac{\partial T}{\partial \mathbf{A}_K} \hat{E}_K E_K^{-1} + 2 \alpha_K \frac{\partial T}{\partial \alpha_K} E_K^{-1} \right) - \frac{(\mathbf{e} \otimes \mathbf{u}) \mathbf{V}}{d+1} \\ &= 2 \rho_K \mathbf{V} \mathbf{J}_K \left(-\frac{1}{2} T \mathbf{I} + \mathbf{A}_K \frac{\partial T}{\partial \mathbf{A}_K} + \alpha_K \frac{\partial T}{\partial \alpha_K} \mathbf{I} \right) \mathbf{J}_K^{-1} - \frac{(\mathbf{e} \otimes \mathbf{u}) \mathbf{V}}{d+1} \\ &= 2 \rho_K \mathbf{V} \mathbf{U} - \frac{(\mathbf{e} \otimes \mathbf{u}) \mathbf{V}}{d+1}, \end{aligned} \tag{35}$$

where $\mathbf{U} = \mathbf{J}_K \left(-\frac{1}{2} T \mathbf{I} + \mathbf{A}_K \frac{\partial T}{\partial \mathbf{A}_K} + \alpha_K \frac{\partial T}{\partial \alpha_K} \mathbf{I} \right) \mathbf{J}_K^{-1}$. By Lemma 4.2, we have

$$\text{tr} \left(\frac{\partial T}{\partial \mathbf{A}_K} \frac{\partial \mathbf{A}_K}{\partial \mathbf{M}_K} \right) = -\mathbf{M}_K^{-1} \mathbf{J}_K^{-T} \frac{\partial T}{\partial \mathbf{A}_K} \mathbf{J}_K^{-1} \mathbf{M}_K^{-1}.$$

Furthermore, we have

$$\frac{\partial \alpha_K}{\partial \mathbf{M}_K} = \det(\mathbf{J}_K^{-1})^2 \frac{\partial \det(\mathbf{M}_K^{-1})}{\partial \mathbf{M}_K} = -\alpha_K \mathbf{M}_K^{-1}.$$

Next, we consider the simplification of $\frac{\partial G}{\partial \mathbf{M}_K}$, and we expand it, then obtain:

$$\begin{aligned}
\frac{\partial G}{\partial \mathbf{M}_K} &= \frac{\partial \rho_K}{\partial \mathbf{M}_K} T + \rho_K \left(\text{tr} \left(\frac{\partial T}{\partial \mathbf{A}_K} \frac{\partial \mathbf{A}_K}{\partial \mathbf{M}_K} \right) + \frac{\partial T}{\partial \alpha_K} \frac{\partial \alpha_K}{\partial \mathbf{M}_K} \right) \\
&= \rho_K \left(\frac{1}{2} T \mathbf{M}_K^{-1} - \mathbf{M}_K^{-1} \mathbf{J}_K^{-T} \frac{\partial T}{\partial \mathbf{A}_K} \mathbf{J}_K^{-1} \mathbf{M}_K^{-1} - \frac{\partial T}{\partial \alpha_K} \alpha_K \mathbf{M}_K^{-1} \right) \\
&= -\rho_K \mathbf{J}_K \left(-\frac{1}{2} T \mathbf{I} + \mathbf{A}_K \frac{\partial T}{\partial \mathbf{A}_K} + \alpha_K \frac{\partial T}{\partial \alpha_K} \mathbf{I} \right) \mathbf{J}_K^{-1} \mathbf{M}_K^{-1} \\
&= -\rho_K \mathbf{U} \mathbf{M}_K^{-1}.
\end{aligned} \tag{36}$$

All the constructs we are concerned with related to a particular functional are now concentrated in the tensor \mathbf{U} . The construction of \mathbf{U} is as simple as the contravariant form.

To demonstrate the simplification of derivatives for a specific functional, we provide the following examples:

Example 4.1 (A-Huang's functional).

$$\begin{cases} T = \mu \text{tr}(\mathbf{A}_K)^{\frac{d\gamma}{2}} + (1-2\mu)d^{\frac{d\gamma}{2}}\alpha_K^{\frac{\gamma}{2}}; \\ \frac{\partial T}{\partial \mathbf{A}_K} = \mu \frac{d\gamma}{2} \text{tr}(\mathbf{A}_K)^{\frac{d\gamma}{2}-1} \mathbf{I}; \\ \frac{\partial T}{\partial \alpha_K} = (1-2\mu)d^{\frac{d\gamma}{2}} \frac{\gamma}{2} \alpha_K^{\frac{\gamma}{2}-1}. \end{cases}$$

Example 4.2 (A-Kolasinski-Huang's functional).

$$\begin{cases} T = \|\mathbf{A}_K - \theta \mathbf{I}\|_F^{2\gamma}; \\ \frac{\partial T}{\partial \mathbf{A}_K} = 2\gamma \|\mathbf{A}_K - \theta \mathbf{I}\|_F^{2\gamma-2} (\mathbf{A}_K - \theta \mathbf{I}); \\ \frac{\partial T}{\partial \alpha_K} = 0. \end{cases}$$

Example 4.3 (The functional proposed in this paper).

$$\begin{cases} T = \text{tr}(\mathbf{A}_K)^{\frac{d\gamma}{2}} - d^{\frac{d\gamma}{2}} \frac{\gamma}{2} \theta^{\frac{d\gamma}{2}} \ln \alpha_K; \\ \frac{\partial T}{\partial \mathbf{A}_K} = \frac{d\gamma}{2} \text{tr}(\mathbf{A})^{\frac{d\gamma}{2}-1} \mathbf{I}; \\ \frac{\partial T}{\partial \alpha_K} = -d^{\frac{d\gamma}{2}} \frac{\gamma}{2} \theta^{\frac{d\gamma}{2}} \alpha_K^{-1}. \end{cases} \tag{37}$$

The three examples above clearly demonstrate that our structure has broad applicability. It only requires the construction of a fairly simple gradient structure, and it unifies the objects to be constructed from both covariant and contravariant perspectives, making it easier to implement overall. Our structure does not fully encompass more complex structures, such as adding $\text{Cof}(\mathbf{A})$, which is represented as a combination of α and \mathbf{A} that can still be handled. Of course, we can also include it in the differential construction term and make corresponding adjustments to equations eq. (34) and eq. (35). This extension is straightforward, and which is beyond our scope.

4.4 Moving Mesh Algorithms

Next, we will explain the relevant content of the contravariant algorithm, including the construction algorithm of the global moving vector field and the gradient flow update algorithm of the contravariant algorithm. At the time step level, a general stiff ODE solver such as the BDF method [8, 2] can be selected, and the update of the moving vector field will be embedded in the ODE solver. In addition, we employ a Newton-Krylov scheme: at each Newton step we solve $(\mathbf{I} - h\mathbf{J}) \Delta = -r$ with CG. The first Newton step assembles \mathbf{J} once to form $\mathbf{J}_{NT} = \mathbf{I} - h\mathbf{J}$; subsequent steps apply low-rank DFP-type updates to \mathbf{J}_{NT}^k and only use matvecs with CG, without maintaining an inverse approximation. Let $\mathbf{s}_k = \Delta_k$ and $\mathbf{t}_k = \mathbf{r}_k - \mathbf{r}_{k-1}$, then

$$\mathbf{J}_{NT}^{k+1} = \mathbf{J}_{NT}^k + \frac{\mathbf{t}_k \mathbf{t}_k^\top}{\mathbf{s}_k^\top \mathbf{t}_k} - \frac{\mathbf{J}_{NT}^k \mathbf{s}_k \mathbf{s}_k^\top \mathbf{J}_{NT}^k}{\mathbf{s}_k^\top \mathbf{J}_{NT}^k \mathbf{s}_k},$$

and we provide the matvec $v \mapsto \mathbf{J}_{NT}^{k+1}v$ to CG. When $s_k^\top t_k$ is too small, we fall back to the good-Broyden (rank-one) update

$$\mathbf{J}_{NT}^{k+1} = \mathbf{J}_{NT}^k + \frac{(\mathbf{t}_k - \mathbf{J}_{NT}^k s_k) s_k^\top}{s_k^\top s_k}.$$

This yields a Jacobian-free, low-memory quasi-Newton acceleration for BDF time stepping; see [7, 4, 17, 24].

Algorithm algorithm 1 provides the core element-level gradient assembly procedure based on the simplified formulas eq. (34) and eq. (37). This assembly process is embedded within the larger gradient flow update framework described below. The element gradients computed by Algorithm algorithm 1 are used to construct the global moving vector field, which drives the mesh evolution in the following complete update algorithm.

The complete moving mesh algorithm (Algorithm algorithm 2) integrates the element gradient assembly (Algorithm algorithm 1) within an iterative time-stepping framework. At each iteration, after constructing the metric matrices and computing invariants, the BDF method advances the computational coordinates. The gradient vector needed for this advancement is assembled by calling Algorithm algorithm 1 for all mesh elements. Finally, the physical mesh and solution are updated through interpolation, completing one full adaptation cycle.

Algorithm 1 Element Gradient Assembly for Single Iteration

Require: For each element K : edge matrices E_K, \hat{E}_K , metric \mathbf{M}_K , and parameters ρ_K, θ

Ensure: Element discrete gradient $\frac{\partial I_K}{\partial [\xi_0^K, \xi_1^K, \dots, \xi_d^K]}$

for each element K in mesh **do**

 Compute $\mathbf{A}_K = \mathbf{J}_K^{-1} \mathbf{M}_K^{-1} \mathbf{J}_K^{-1}$, where $\mathbf{J}_K = E_K \hat{E}_K^{-1}$

 Compute $\alpha_K = \det(\mathbf{A}_K)$, $\text{tr}(\mathbf{A}_K)$

 Compute tensor derivatives $\frac{\partial T}{\partial \mathbf{A}_K}$ and $\frac{\partial T}{\partial \alpha_K}$ using (32)

 Compute element gradient using (29): $\frac{\partial I_K}{\partial [\xi_0^K, \dots, \xi_d^K]} = 2\rho_K \mathbf{R} \hat{E}_K^{-1} (\mathbf{A}_K \frac{\partial T}{\partial \mathbf{A}_K} + \alpha_K \frac{\partial T}{\partial \alpha_K} \mathbf{I})$

end for

Remark 4.2. The assembly method for \mathbf{x} -view will not be discussed here. Its update amount is different from that of contravariants, and constructing the \mathbf{U} tensor is beneficial to reduce construction costs.

Algorithm 2 ξ -view Gradient Flow Update Algorithm

Require: Initial computational coordinates ξ^0 , total iteration count $iter$, single-step time interval t_{span} , single-step iteration count n_t , relative tolerance $rtol$, absolute tolerance $atol$

Ensure: Moved physical mesh \mathcal{T}_h

Initialize $\xi^n = \xi^0$, time step $\Delta t = t_{span}/n_t$

Construct initial logical mesh

for $i = 1$ to $iter$ **do**

Outer initialization:

 Construct piecewise constant metric matrices \mathbf{M} (including metric construction and smoothing)

 Compute and cache single-step invariants: physical mesh edge matrices $E_K, \mathbf{M}^{-1}, \rho, \mathbf{P}$, and θ

BDF integration:

 Integrate ξ to t_{span} using BDF method with step Δt , tolerances $rtol, atol$

 Obtain updated computational coordinates ξ^{n+1}

 Assemble global vector using Algorithm 1

Mesh and solution update:

 Construct new physical mesh points \mathbf{x}^{n+1} via linear interpolation

 Interpolate physical quantities to new mesh via linear interpolation

 Update information on the new mesh

 Set $\xi^n = \xi^{n+1}$ for next iteration

end for

return Final computed physical mesh \mathcal{T}_h with coordinates \mathbf{x}

5 Numerical Experiments

5.1 Experimental Setup

We adopt a uniform setup for all numerical experiments: the computational and physical domains coincide ($\Omega_c = \Omega_p$) and are discretized with staggered triangular meshes. Unless noted, we use a Newton-Krylov solve with a DFP-updated linear operator and CG inner iterations, with a tolerance of 10^{-6} on the nonlinear iterations.

Because [20] shows that functionals eq. (16) and eq. (17) perform similarly, we use Huang's functional eq. (12) as a representative benchmark, which is widely used in the literature.

We test three metric tensors, each targeting different features and anisotropy. Not every metric suits every problem; unsuitable choices can cause distortion or under-resolution, therefore, such cases are intentionally excluded from the comparison.

Hessian-based type:

$$\mathbf{M}_K = \det(|\mathbf{H}_K(u)|)^{-\frac{1}{d+4}} |\mathbf{H}_K(u)| \quad (38)$$

This is the standard Hessian-based metric, where \mathbf{H}_K is the pointwise Hessian matrix recovered via least-squares fitting of function values, and $|\mathbf{H}_K| = \mathbf{Q}\Lambda\mathbf{Q}^T$, $\Lambda = \text{diag}(|\lambda_1|, \dots, |\lambda_d|)$, with λ_i being the eigenvalues of the Hessian matrix. The derivation of this class of metrics has been thoroughly discussed in [14].

Arc-length-like type:

$$\mathbf{M}_K = \sqrt{1 + \beta |\nabla u_h|^2} \mathbf{I} \quad (39)$$

where $\beta \geq 0$ is a control parameter. This isotropic metric has been validated for its effectiveness in various studies. For functionals that simultaneously require equidistribution and alignment, its distribution requirements are often more stringent. It has been discussed and applied in [26, 22].

Eigen-decomposition type:

$$\mathbf{M}_K = \lambda_1 \mathbf{v}(\mathbf{v})^T + \lambda_2 \mathbf{v}^\perp (\mathbf{v}^\perp)^T, \quad (40)$$

where \mathbf{v} and \mathbf{v}^\perp are mutually orthogonal unit eigenvectors constructed as

$$\mathbf{v} = \frac{\nabla u_h}{\|\nabla u_h\|}, \quad \lambda_1 = 1 + \alpha\psi, \quad \alpha = \frac{\beta}{\langle \psi \rangle (1 - \beta)}.$$

Here, $\langle \cdot \rangle$ denotes the domain average, $\beta \in (0, 1)$ is a user-defined parameter, and $\psi = \sqrt{1 + \|\nabla u\|^2} - 1$. This functional exhibits anisotropic properties and has been presented and validated in [9].

The following tests will select from these three metric types. For the construction of the metric tensor, this paper will not delve into the related details; readers may refer to [15, 11].

The first test involves mesh distribution directly induced by a function, for which the representative Hessian type is sufficient as it controls static interpolation error and serves as a good test subject. The second test is the numerical solution of Burgers' equation with an exact solution, where the arc-length-like type eq. (39) is a common benchmark; additionally, eq. (38) is included for comparison. The third test simulates Rayleigh-Taylor instability, which is more suited to anisotropic distribution; thus, both eq. (38) and eq. (40) will be employed.

Furthermore, in the subsequent tests, the stretching factor $\kappa = (d^{\frac{d\gamma}{2}} \theta^{\frac{d\gamma}{2}} (1 - \frac{d\gamma}{2} \ln \theta))^{-1}$ is used as the lower-bound scaling for our proposed functional. Considering that the dimension is influenced by \mathbf{M}_K and θ also carries dimension, we define $[\mathbf{M}] = \sqrt{\theta^{-1/2} \det(\mathbf{M})^{1/d}}$. The balancing function for our functional can be constructed as $P_i = [\mathbf{M}]^{-\frac{d}{2}}$, while for functional eq. (12) the balancing function is given as $P_i = \det(\mathbf{M})^{\frac{p-1}{2}}$.

Parameter choices: For the proposed functional, we use $\gamma = 1.25$ and $\tau = 0.004$, chosen via preliminary convergence studies and stability analysis. Huang's functional employs $\gamma = 3/2$ and $\tau = 0.01$ (standard choices from literature). Both use BDF time integration.

All numerical experiments are implemented using FEALPy [31], a multi-backend simulation library that offers flexible mesh data structures and supports high-order finite element discretizations. The computational meshes and solution fields are visualized using ParaView.

5.2 Mesh Distribution Induced by the Two-Dimensional Functions

To quantitatively evaluate the quality of the generated meshes, we adopt three types of evaluation metrics consistent with those in the literature [12, 20]: equidistribution Q_{eq} , alignment Q_{ali} , and geometric quality Q_{geo} . The geometric

quality metric primarily characterizes the shape quality and aspect ratio of mesh elements, i.e., the degree of anisotropy of elements in Euclidean space.

The overall statistics of the above metrics are computed as the root mean square of the element-wise quantities Q_K , defined as:

$$Q = \sqrt{\frac{1}{NC} \sum_{K \in \mathcal{T}_c} Q_K^2},$$

where NC denotes the number of elements and \mathcal{T}_c represents the computational mesh. Specifically, the element-wise metrics are defined as follows:

$$Q_{eq,K} = \frac{|K| \det(\mathbf{M}_K)^{\frac{1}{2}}}{\sigma_h/NC}, Q_{ali,K} = \frac{\text{tr}(\mathbf{J}_K^T \mathbf{M}_K \mathbf{J}_K)}{d \det(\mathbf{J}_K^T \mathbf{M}_K \mathbf{J}_K)^{\frac{1}{d}}}, Q_{geo,K} = \frac{\text{tr}(\mathbf{J}_K^T \mathbf{J}_K)}{d \det(\mathbf{J}_K^T \mathbf{J}_K)^{\frac{1}{d}}}.$$

Here, $Q_{eq,K}$ measures the equidistribution of element volumes in the metric space, $Q_{ali,K}$ describes the alignment between the element and the given metric tensor, and $Q_{geo,K}$ reflects the shape quality of the element. For element-wise statistics, we employ $1/Q_{ali,K}$ as the criterion to intuitively present the local alignment level of elements.

In terms of numerical validation, we first conduct systematic assessments of the aforementioned quality metrics through mesh distribution experiments induced by several functions with significant gradients or singular features. Furthermore, we focus on examining the numerical manifestations of the theoretical conclusions presented in Section 4, including: the positivity of the lower bound on element volume and the decreasing trend of the discrete energy functional during the iterative process.

Example 5.1. *In this example, we consider a two-dimensional function with a sinusoidally modulated steep gradient region, defined by*

$$f = \tanh(-100(y - 0.5 - 0.25 \sin(2\pi x))), \quad (x, y) \in [0, 1] \times [0, 1]$$

The moving mesh equations are integrated up to $t = 1$ using a time step size of 0.05.

Figure fig. 2 illustrates the mesh distribution induced by the proposed functional, demonstrating effective adaptation to both geometric shape and local scale variations. Consistent with the Hessian-based metric, elements are significantly refined in regions of large curvature, while remaining naturally sparser along the centerline of the high-gradient band where curvature is small.

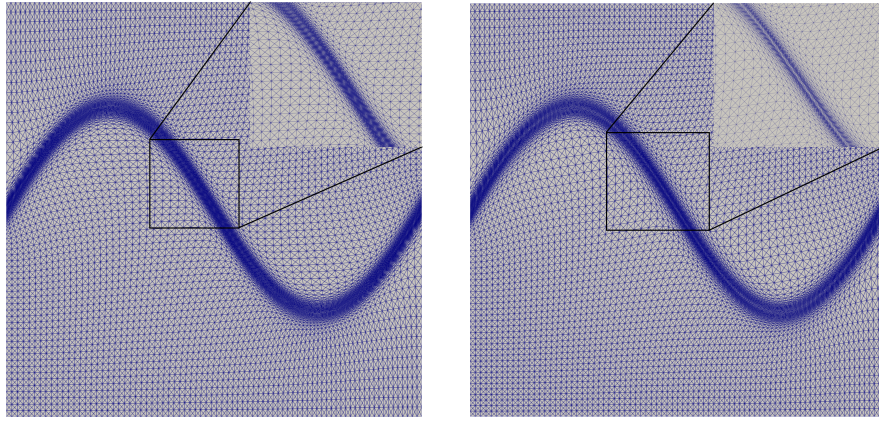
Table 1 reports global mesh quality measures, interpolation errors, and computational times. The results indicate that the proposed functional exhibits superior equidistribution, consistently outperforming Huang's functional. Although alignment quality is slightly weaker, interpolation errors remain comparable, with the proposed method achieving marginally smaller errors in most cases. Furthermore, the proposed functional substantially reduces computational cost under the Newton-Krylov solver with a DFP-updated operator and CG. Both functionals demonstrate good adaptability to anisotropy regarding geometric skewness.

Figure fig. 3 presents histograms of element-wise quality measures. The distributions for the proposed functional cluster tightly around unity, confirming its superior equidistribution. In contrast, Huang's functional shows a relative advantage in handling poorly aligned elements, consistent with Table 1. Finally, the monotonic decrease in the functional value shown in Figure fig. 4 aligns with the theoretical analysis in Section 3.

Table 1: mesh quality metrics, interpolation errors, and computational times for the function in Example 5.1.

| functional | size(NC) | Q_{eq} | Q_{ali} | Q_{geo} | e_{L_2} | time(s) | steps |
|------------|----------|----------|-----------|-----------|-----------|---------|-------|
| Huang | 1600 | 1.10546 | 1.08201 | 2.45353 | 0.01240 | 5.177 | 1314 |
| | 6400 | 1.12450 | 1.07075 | 3.45254 | 0.00207 | 23.786 | 1243 |
| | 25600 | 1.19353 | 1.05530 | 2.84693 | 0.00054 | 180.276 | 1176 |
| Ours | 1600 | 1.07717 | 1.10908 | 2.73628 | 0.01087 | 3.484 | 901 |
| | 6400 | 1.07822 | 1.11457 | 3.73199 | 0.00185 | 17.627 | 922 |
| | 25600 | 1.11586 | 1.11713 | 2.99694 | 0.00047 | 160.535 | 1007 |
| Ours-DFPCG | 25600 | 1.11772 | 1.11717 | 2.96763 | 0.00048 | 26.631 | — |

Remark 5.1 (Computational cost). *Computation times are measured on an Intel Core i7-12700K CPU with 16GB RAM, using FEALPy with Python 3.13 and NumPy with OpenBLAS backend. Times include metric construction, functional evaluation, and the Newton-Krylov solve with DFP-updated operator and CG. The column "steps" reports the total number of nonlinear iteration steps.*



(a) Mesh distribution using the proposed functional.
(b) Mesh distribution using Huang's functional.

Figure 2: Mesh distribution induced by the function in Example 5.1 using the proposed functional and Huang's functional with 25600 elements.

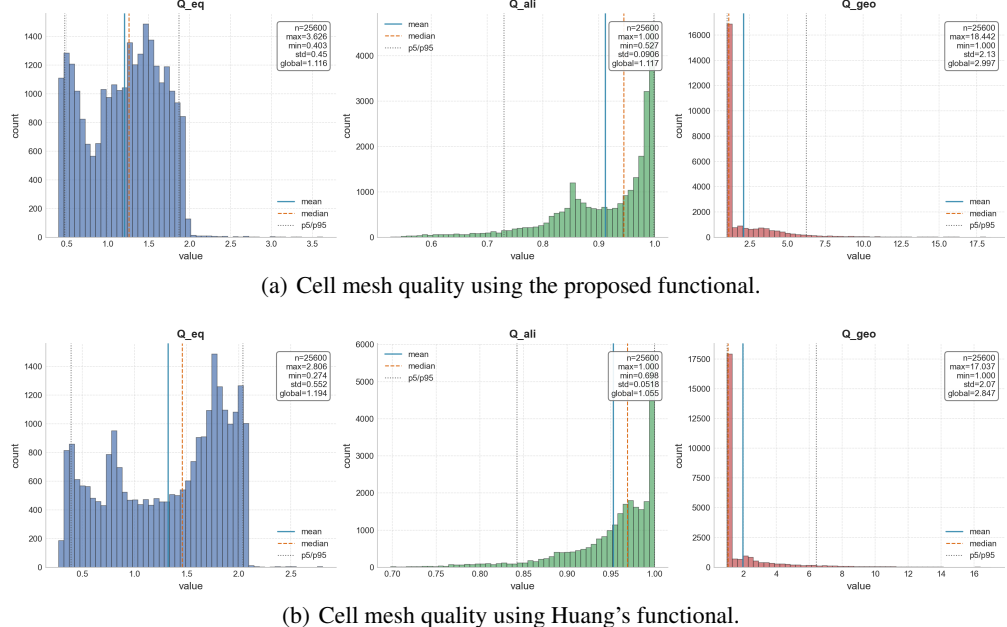


Figure 3: Cell mesh quality distributions induced by the function in Example 5.1 using the proposed functional and Huang's functional with 25600 elements.

Example 5.2. *In this example, we consider a function featuring an X-shaped high-gradient region, which combines line-type anisotropic structures with pointwise isotropic behavior at the intersection. The function is defined as*

$$f = \tanh(100(1 - x - y)) - \tanh(100(x - y)), \quad (x, y) \in [0, 1] \times [0, 1]$$

Such a configuration poses a challenging test for mesh adaptation, as the dominant gradient directions vary abruptly in space and transition from strongly anisotropic features to nearly isotropic behavior at the crossing point. The moving mesh equations are integrated up to $t = 1$ with a time step size of 0.1.

Figure 5 shows the mesh distribution with local magnifications: elements follow the two intersecting high-gradient lines and become nearly isotropic near the intersection, with smooth transition and no noticeable distortion, indicating good regularity. The transition between anisotropic and isotropic regions is smooth, and no excessive mesh distortion is observed, indicating good mesh regularity and smoothness.

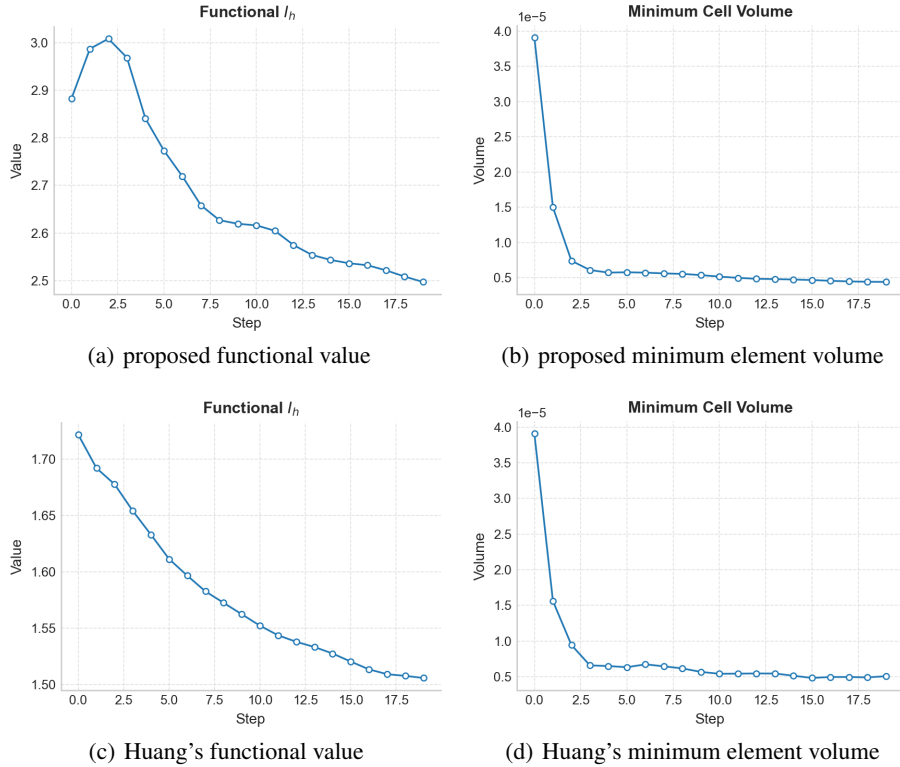


Figure 4: Evolution of the mesh functional value and minimum element volume for the function in Example 5.1 using the proposed functional and Huang's functional with 25600 elements.

Table 2 shows trends similar to Example 5.1: the proposed functional yields stronger equidistribution, Huang's gives slightly better alignment on finer meshes, and both deliver comparable interpolation errors, indicating that the proposed method maintains accuracy despite the reduced emphasis on alignment.

Figure 6 illustrates the evolution of the mesh functional value under the chosen time step. The results show a clear monotonic decrease of the functional, together with a well-defined lower bound on the element size, which is consistent with the observations made in Example 5.1.

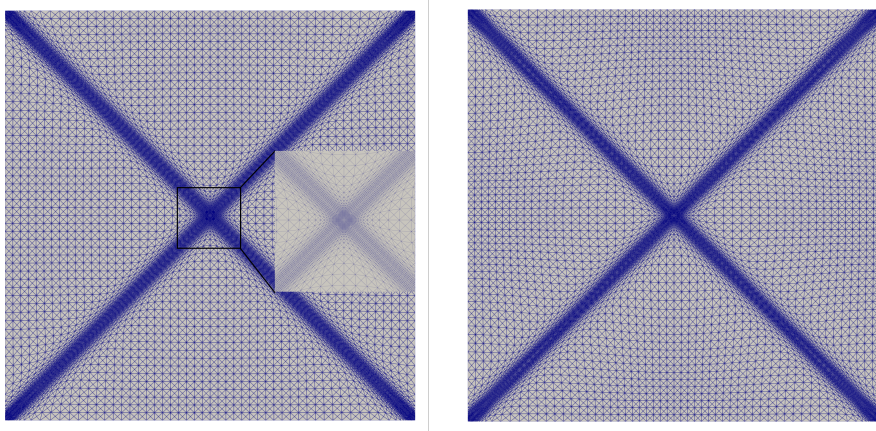
Table 2: mesh quality metrics, interpolation errors, and computational times for the function in Example 5.2 (X-shaped test).

| functional | size(NC) | Q_{eq} | Q_{ali} | Q_{geo} | e_{L_2} | time(s) | steps |
|------------|----------|----------|-----------|-----------|-----------|---------|-------|
| Huang's | 1600 | 1.05390 | 1.08719 | 2.97354 | 0.01189 | 2.967 | 673 |
| | 6400 | 1.06317 | 1.11351 | 5.36236 | 0.00117 | 16.604 | 996 |
| | 25600 | 1.01954 | 1.07369 | 4.14143 | 0.00045 | 137.527 | 1155 |
| Ours | 1600 | 1.03158 | 1.06869 | 2.66552 | 0.01429 | 2.343 | 634 |
| | 6400 | 1.04189 | 1.09445 | 4.28840 | 0.00140 | 12.744 | 717 |
| | 25600 | 1.01511 | 1.12212 | 3.48463 | 0.00043 | 94.519 | 658 |
| Ours-DFPCG | 25600 | 1.01525 | 1.15684 | 3.38729 | 0.00042 | 22.200 | – |

5.3 Numerical Solution of the Two-Dimensional Burgers' Equation

Example 5.3. We consider the scalar Burgers' equation

$$\begin{cases} \frac{\partial u}{\partial t} + uu_x + uu_y = \frac{1}{Re} \Delta u, & \text{in } \Omega = [0, 1] \times [0, 1]; \\ u = g, & \text{on } \partial\Omega; \\ u(\mathbf{x}, 0) = u_0, \end{cases} \quad (41)$$



(a) Mesh distribution using the proposed functional.
(b) Mesh distribution using Huang's functional.

Figure 5: Mesh distribution induced by the function in Example 5.2 using the proposed functional and Huang's functional with 25600 elements.

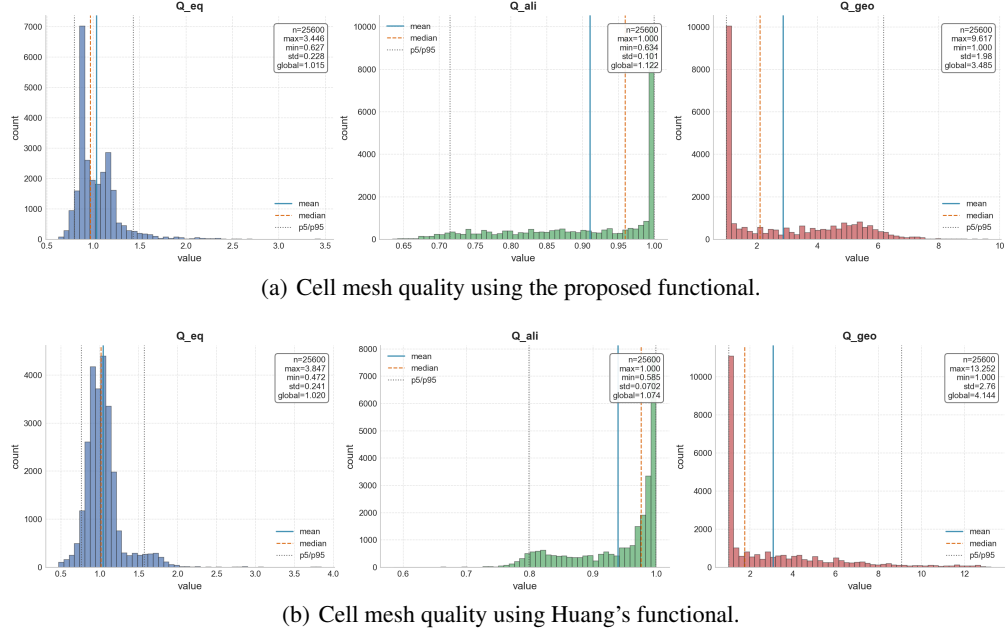


Figure 6: Cell mesh quality distributions induced by the function in Example 5.2 using the proposed functional and Huang's functional with 25600 elements.

The problem admits the exact solution

$$u = \frac{1}{1 + \exp(Re(x + y - t))}.$$

Time integration uses the SDIRK2 scheme on $T = [0, 2]$ with uniform step 0.002, and a moving mesh of 3600 elements. We compare the impact of two control functions, eq. (38) and eq. (39), on solution accuracy while keeping all other settings identical to the previous experiments.

Figures 8 and 9 present the mesh distributions at $t = 0.5, 1.0$, and 1.5 , respectively. It can be observed that both control functions successfully guide the mesh to align and concentrate along the characteristic line $x + y = t$, with pronounced stretching in the tangential direction and compression in the normal direction. In particular, the Hessian-based control function exhibits a stronger mesh concentration effect, which is consistent with its inherent capability of capturing anisotropic features of the solution.

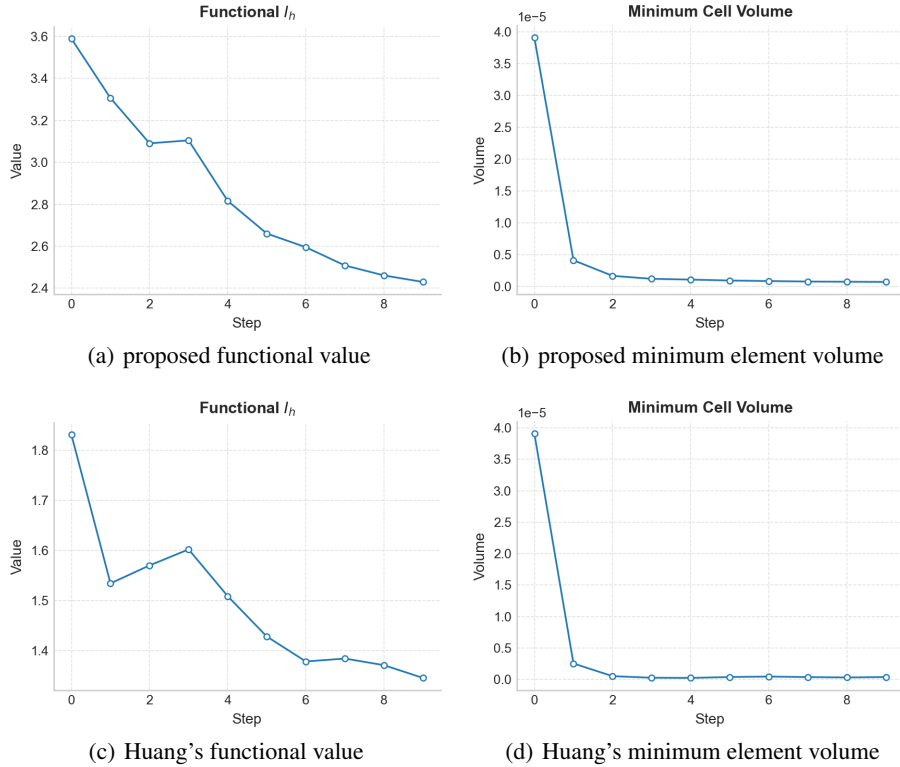


Figure 7: Evolution of the mesh functional value and minimum element volume for the function in Example 5.2 using the proposed functional and Huang's functional with 25600 elements.

Figure 10 compares the L_2 and H_1 error histories obtained using the two control functions. For reference, we also include the results produced by Huang's functional eq. (16) combined with the control function eq. (39). The results indicate that the proposed functional consistently yields slightly smaller errors than Huang's functional. More importantly, the Hessian-based metric leads to a noticeable improvement in accuracy for this problem, outperforming the arc-length-type metric throughout the entire time interval. The quantitative results reported in Table 3 further confirm these observations. At all reported time instances, the Hessian-based metric achieves the best accuracy among the tested configurations. It is worth noting that, at the initial and final stages, mesh points tend to cluster near boundary corner regions, where the solution exhibits corner singularities. Nevertheless, the proposed functional remains numerically stable and robust under such conditions, without exhibiting any deterioration in convergence behavior.

Table 3: L_2 and H_1 errors for Burgers' equation (Example 5.3).

| functional | Error type | t (s) | | | | |
|----------------------|------------|----------|----------|----------|----------|----------|
| | | 0 | 0.5 | 1.0 | 1.5 | 2.0 |
| Ours (Arc-Length) | | 5.46e-04 | 2.08e-03 | 2.56e-03 | 1.79e-03 | 3.26e-04 |
| Huang's (Arc-Length) | L_2 | 7.43e-04 | 2.71e-03 | 3.51e-03 | 2.52e-03 | 4.66e-04 |
| Ours (Hessian) | | 6.06e-05 | 6.52e-04 | 8.05e-04 | 7.94e-04 | 4.76e-05 |
| Ours (Arc-Length) | | 1.20e-01 | 5.67e-01 | 8.02e-01 | 6.04e-01 | 1.10e-01 |
| Huang's (Arc-Length) | H_1 | 1.39e-01 | 6.33e-01 | 8.36e-01 | 6.31e-01 | 1.31e-01 |
| Ours (Hessian) | | 3.82e-02 | 3.11e-01 | 2.48e-01 | 4.43e-01 | 4.04e-02 |

5.4 Rayleigh-Taylor Instability Test

The Rayleigh-Taylor instability is employed here as a representative benchmark featuring strong nonlinearity and pronounced multiscale behavior, in order to assess the practical performance of the proposed mesh functional. Our objective is not to conduct a detailed investigation of Rayleigh-Taylor dynamics themselves, but rather to demonstrate that the proposed functional remains robust and effective in flows involving interface roll-up and the formation of moderate vortical structures.

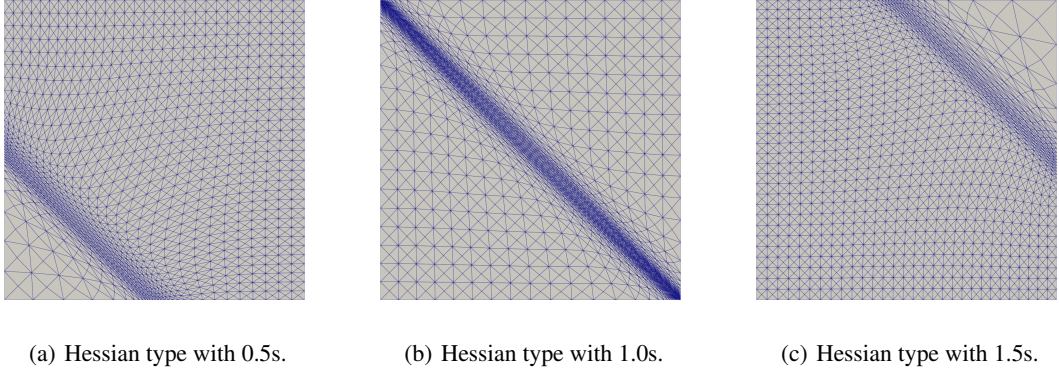


Figure 8: The mesh distributions for the Burgers' equation solution using our functional combined with the Hessian-based metric are shown from left to right at times $t = 0.5$ s, 1 s, and 1.5 s.

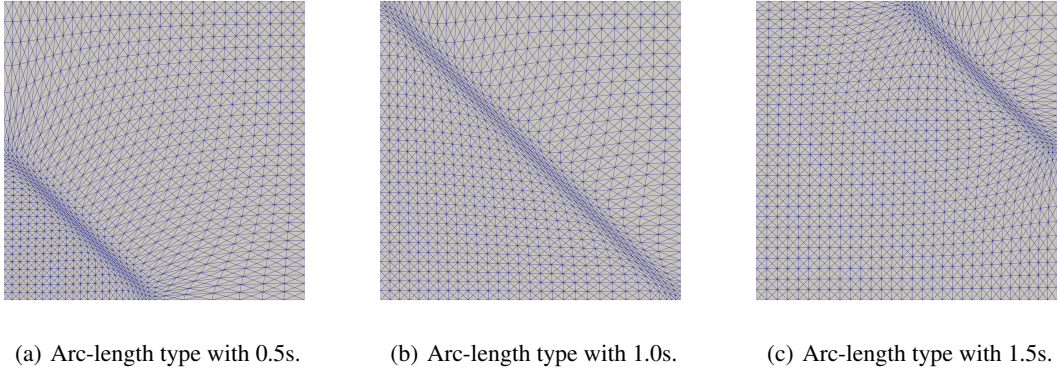


Figure 9: The mesh distributions for the Burgers' equation solution using our functional combined with the Arc-length-based metric are shown from left to right at times $t = 0.5$ s, 1 s, and 1.5 s.

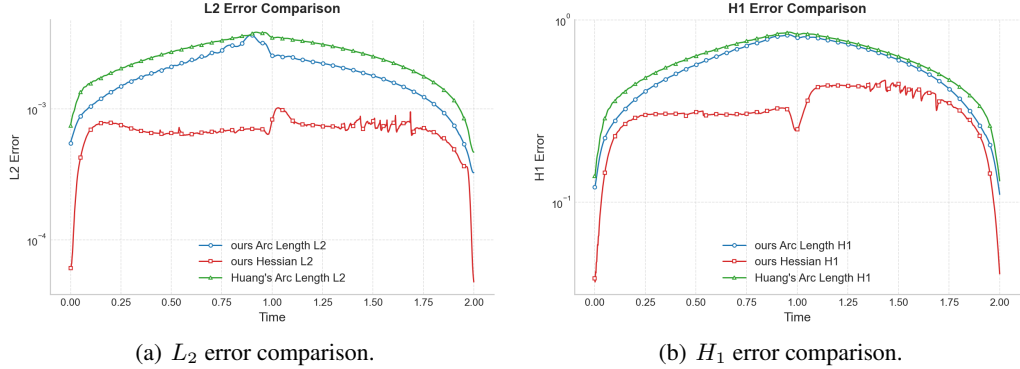


Figure 10: The time histories of the L_2 (a) and H_1 (b) errors for our functional and Huang's functional, under both the arc-length-based and Hessian-based metrics, are compared in the left and right panels, respectively.

Owing to the anisotropic nature of the flow features and the presence of vortical structures evolving in multiple directions, tensor-based metrics constructed from Hessian information or eigen-decomposition are more suitable for this problem. In contrast, purely arc-length-based control does not align well with the distribution constraints imposed by the present mesh functional. Consequently, metrics eq. (38) and eq. (40) are adopted in this test to evaluate the adaptive capabilities of the proposed approach.

Example 5.4. *The flow is modeled by the Cahn-Hilliard-Navier-Stokes system:*

$$\begin{cases} \rho(\phi) \left(\frac{\partial \mathbf{u}}{\partial t} + (\mathbf{u} \cdot \nabla) \mathbf{u} \right) = -\nabla p + \eta \Delta \mathbf{u} + \rho(\phi) \mathbf{g}, & \text{in } \Omega_p \times (0, T], \\ \nabla \cdot \mathbf{u} = 0, & \text{in } \Omega_p \times (0, T], \\ \frac{\partial \phi}{\partial t} + \nabla \cdot (\phi \mathbf{u}) = M \Delta \phi, & \text{in } \Omega_p \times (0, T], \\ \phi = \alpha \phi^3 - \beta \phi - k \Delta \phi, & \text{in } \Omega_p \times (0, T]. \end{cases}$$

The system is supplemented with the following initial and boundary conditions:

$$\begin{cases} \mathbf{u} = \mathbf{g}_u, \quad \phi = g_\phi, & \text{on } \Gamma_u \times (0, T], \\ p = g_p, & \text{on } \Gamma_p \times (0, T], \\ \mathbf{u}(\cdot, 0) = \mathbf{u}_0, \quad \phi(\cdot, 0) = \phi_0, & \text{in } \Omega_p. \end{cases}$$

The density is defined as a phase-dependent mixture

$$\rho(\phi) = \rho_1(1 - \phi)/2 + \rho_2(1 + \phi)/2,$$

and the gravitational acceleration is given by $\mathbf{g} = (0, -g)$.

The physical domain is defined as $\Omega_p = [0, 1] \times [0, 2]$. At the initial time, the interface between the two immiscible fluids is located along the horizontal line $y = 1$, perturbed by a cosine disturbance to trigger the Rayleigh-Taylor instability. The initial phase-field variable is given by

$$\phi(x, y, 0) = \tanh \left(\frac{y - 1 - 0.1 \cos(2\pi x)}{\sqrt{2}\varepsilon} \right).$$

The density parameters are chosen as $\rho_0 = 2$ and $\rho_1 = 1$. The governing system is discretized following the framework and nondimensionalization strategy proposed in [21], leading to the parameter values

$$Re = 3000, \quad Fr = 1, \quad \varepsilon = 0.005, \quad Pe = 100/\varepsilon$$

As reported in [21], larger values of the Peclet number Pe promote the development of more pronounced vortex structures during the nonlinear stage of the instability.

For time integration, a BDF2 scheme is employed [8]. The second-order approximation of the mesh velocity is given by $\dot{\mathbf{x}} = \frac{3\mathbf{x}^{n+1} - 4\mathbf{x}^n + \mathbf{x}^{n-1}}{2\Delta t}$, with a time step size $\Delta t = 0.005 \times 0.16\sqrt{2}$.

Spatial discretization is carried out using the finite element method on an initial mesh consisting of 14,112 triangular elements. Quadratic elements are used for both the phase-field and velocity variables, while linear elements are adopted for the pressure.

This test is designed to evaluate the ability of the proposed functional and moving mesh algorithm to accurately capture complex interface evolution in a physically relevant setting, particularly in the presence of small-scale flow structures.

Figure 11 presents the simulation results at $t = 2.75$ s, where Figure 11(a) and Figure 11(c) display the interface shapes, and Figure 11(b) and Figure 11(d) illustrate the corresponding mesh distributions. In both cases, the evolving interface is well resolved, demonstrating that the proposed approach effectively adapts the mesh to the dynamics of the Rayleigh-Taylor instability.

It is evident that metric eq. (40) drives a stronger concentration of mesh elements toward the interface compared to metric eq. (38), which yields a smoother distribution. This difference in adaptivity is further highlighted in the magnified views of the roll-up structures in Figure 12. Under metric eq. (40), fine-scale features are resolved more sharply, illustrating the trade-off between mesh smoothness and the intensity of local adaptation.

As observed in Figures 11(a) and 11(c), the interface shapes exhibit slight differences depending on the metric tensor employed. Such discrepancies are expected in Rayleigh-Taylor simulations, as the interface evolution is sensitive to

the underlying mesh distribution and numerical dissipation. However, the overall evolution trends—such as the growth rate of the rising spikes—remain largely consistent, with differences mainly confined to the fine-scale roll-ups shown in Figure 12. Importantly, no nonphysical interface breakup, self-intersection, or spurious numerical oscillations are observed in any of the simulations, confirming the robustness of the proposed method.

Finally, Figure 13 compares the vertical positions of the two-phase spikes obtained using the present moving mesh approach and a reference h -adaptive method. The results show that, under the Hessian-based metric, the rising spike reaches a slightly higher position, while the eigen-decomposition-based metric yields spike locations that are very close to those obtained with h -adaptivity. For the descending flow, all three approaches exhibit nearly identical behavior.

It is worth noting that the reference h -adaptive simulation adopts a relatively conservative refinement strategy and uses the same physical parameters, making it a reliable benchmark. However, it requires approximately twice the computational time of the moving mesh method, highlighting the efficiency advantage of the proposed approach.

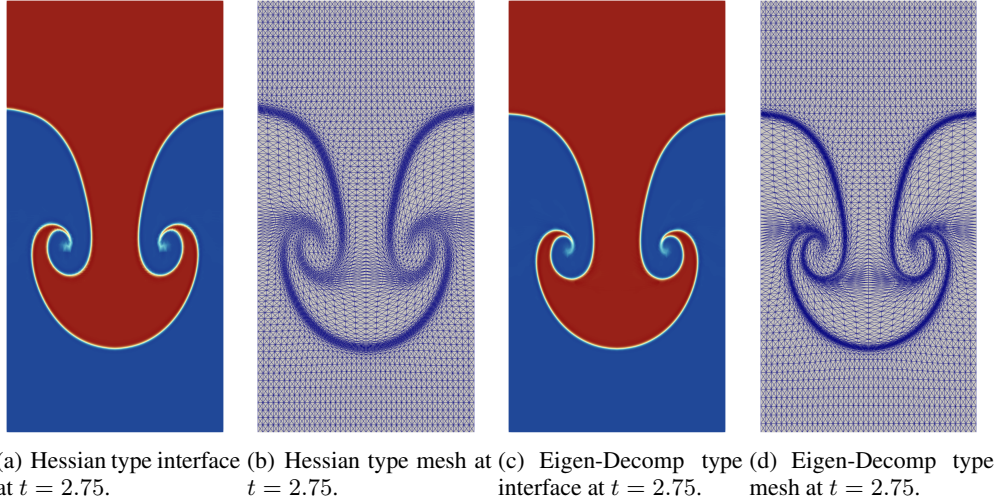


Figure 11: The interface and mesh distribution at time 2.75 s. (a) and (c) display the interfaces obtained using the Hessian-based metric and the eigen-decomposition-based metric, respectively, while (b) and (d) show the corresponding mesh distributions under the Hessian-based metric and the eigen-decomposition-based metric.

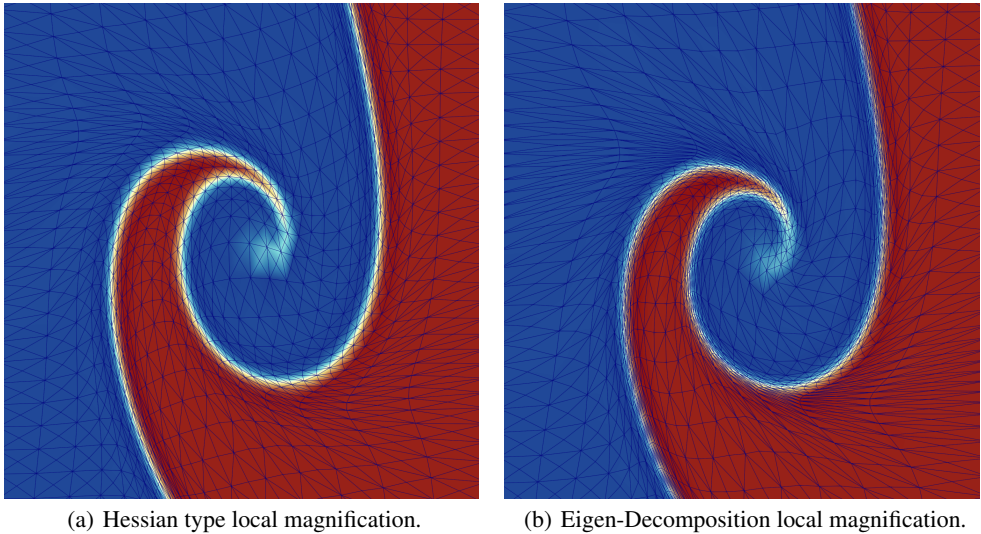
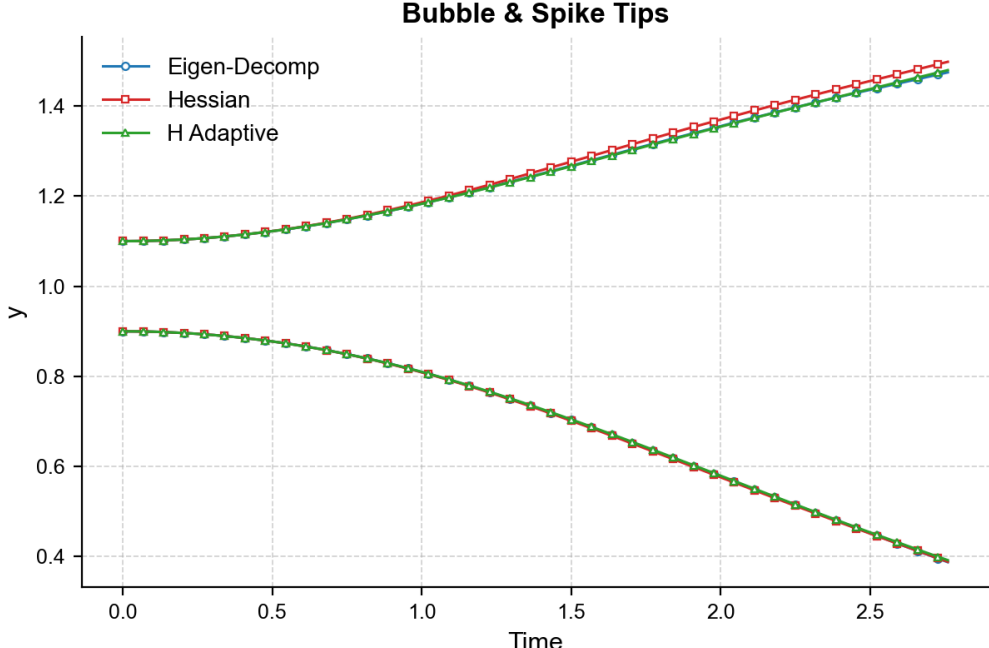
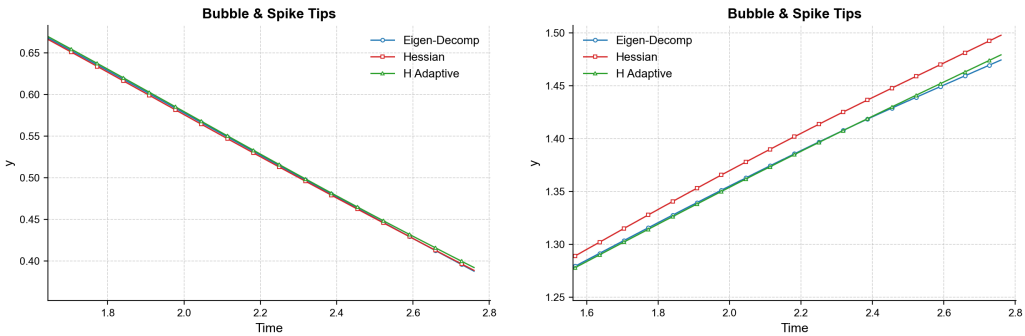


Figure 12: Local magnifications at the roll-up structure, with the left panel corresponding to the Hessian-based metric and the right panel to the eigen-decomposition-based metric.



(a) The y-coordinate of the tip of the falling and rising fluid.



(b) Magnified view of the tip position for the descending fluid. (c) magnified view of the tip position for the ascending fluid.

Figure 13: The y-coordinate of the tip of the falling and rising fluid versus dimensionless time. The green curve represents the results from the h-adaptive method, while the red and blue curves correspond to the moving mesh results under the Hessian-based and eigen-decomposition-based metrics, respectively.

6 Conclusions and Future Work

In this work, we have proposed a new variational functional for adaptive moving mesh generation that provides a unified treatment of equidistribution and alignment within a single energy formulation. The functional is designed to reduce excessive nonlinearity commonly present in existing approaches while preserving the essential geometric and metric-driven adaptation properties. We established several key theoretical properties of the proposed functional, including coercivity, favorable convexity properties, and non-singularity of the resulting mesh transformation, which together ensure the well-posedness and robustness of the variational mesh adaptation process.

On the discretization level, a concise and structure-consistent geometric framework was developed for simplicial meshes, leading to explicit and efficient discrete mesh equations. A quasi-Newton-based optimization strategy, combined with a multilevel moving mesh approach, was employed to improve the efficiency of the nonlinear solution process.

Numerical experiments, including metric-induced adaptive mesh examples and simulations of the Rayleigh-Taylor instability, demonstrate that the proposed method achieves effective equidistribution and alignment, and exhibits robust performance.

Despite these advantages, the current formulation and discretization are primarily tailored to simplicial elements, which may limit direct applicability to quadrilateral, hexahedral, or more general polygonal and polyhedral meshes. Extending the proposed functional and its geometric discretization to more general element types and higher-order finite element frameworks remains an important direction for future research. Further work will also explore tighter coupling with finite element solvers, as well as integration with more flexible discretization paradigms, such as discontinuous Galerkin methods and mesh adaptation on evolving manifolds.

Acknowledgments

This work was supported in part by the 111 Project (No. D23017) and the Program for Science and Technology Innovative Research Team in Higher Educational Institutions of Hunan Province of China; by the National Key R&D Program of China (2024YFA1012600); by the National Natural Science Foundation of China (Grant Nos. 12371410, 12261131501); and by the High Performance Computing Platform of Xiangtan University.

Appendix

A Code Availability and Implementation Details

The implementation is available at <https://github.com/weihuayi/fealpy.git> (branch: `develop`). The moving-mesh routines reside in `fealpy.mmesh.metrictensoradaptive`.

Representative examples demonstrating the usage of the proposed method can be found in the `example/meshopt/mmsh` directory of the repository, including:

- `mmesher_with_solution.py`: Basic moving mesh workflow with a known solution (Section 5.2)
- `scalar_burgers_mm_solver.py`: Burgers' equation test case (Section 5.3)
- `rayleightaylor_mm_solver.py`: Rayleigh-Taylor instability (Section 5.4)

B Proofs of Auxiliary Lemmas

Proof of Lemma 4.1. Let $(AMA^T)_{ij} = A_{im}M_{mn}A_{nj}^T$, where M and G are symmetric. Compute the componentwise derivative with respect to A_{kl}^T :

$$\frac{\partial(AMA^T)_{ij}}{\partial A_{kl}^T} = \frac{\partial(A_{im}M_{mn}A_{nj}^T)}{\partial A_{kl}^T} = A_{im}M_{mn}\delta_{nk}\delta_{jl} + \delta_{il}\delta_{mk}M_{mn}A_{nj}^T.$$

Contract with G_{ij} :

$$\begin{aligned} H_{kl} &:= G_{ij} \frac{\partial(AMA^T)_{ij}}{\partial A_{kl}^T} = G_{ij}(A_{im}M_{mn}\delta_{nk}\delta_{jl} + \delta_{il}\delta_{mk}M_{mn}A_{nj}^T) \\ &= G_{lj}A_{im}M_{mk} + G_{il}M_{kn}A_{nj}^T = M_{km}A_{mi}^TG_{il} + M_{kn}A_{nj}^TG_{lj}. \end{aligned}$$

Using the symmetry of M and G (i.e., $M_{km} = M_{mk}$, $G_{il} = G_{li}$), the two terms are equal, hence

$$H_{kl} = 2M_{kn}A_{nj}^TG_{lj} = (2MA^TG)_{kl}.$$

Therefore,

$$\text{tr}\left(G \frac{\partial(AMA^T)}{\partial A^T}\right) = 2MA^TG.$$

□

Proof of Lemma 4.2. Write $(AM^{-1}A^T)_{ij} = A_{im}M_{mn}^{-1}A_{nj}^T$. We first obtain the componentwise identity for the inverse:

$$\frac{\partial M_{rs}^{-1}}{\partial M_{kl}} = -M_{rk}^{-1}M_{ls}^{-1},$$

which follows from $M_{rs}^{-1}M_{sm} = \delta_{rm}$ by differentiating with respect to M_{kl} in index form. Then

$$\frac{\partial(AM^{-1}A^T)_{ij}}{\partial M_{kl}} = A_{ir} \frac{\partial M_{rs}^{-1}}{\partial M_{kl}} A_{sj}^T = -A_{ir}M_{rk}^{-1}M_{ls}^{-1}A_{sj}^T.$$

Contract with G_{ij} :

$$\begin{aligned} H_{kl} &:= G_{ij} \frac{\partial(AM^{-1}A^T)_{ij}}{\partial M_{kl}} = -G_{ij} A_{ir} M_{rk}^{-1} M_{ls}^{-1} A_{sj}^T \\ &= -M_{rk}^{-1} (A^T GA)_{rs} M_{ls}^{-1} = -(M^{-1} A^T G A M^{-1})_{kl}. \end{aligned}$$

Therefore,

$$\text{tr}\left(G \frac{\partial(AM^{-1}A^T)}{\partial M}\right) = -M^{-1} A^T G A M^{-1}.$$

□

References

- [1] T. Apel. *Anisotropic Finite Elements: Local Estimates and Applications*. Teubner, Stuttgart, 1999.
- [2] U. M. Ascher and L. R. Petzold. *Computer Methods for Ordinary Differential Equations and Differential-Algebraic Equations*. SIAM, Philadelphia, 1998.
- [3] J. M. Ball. Convexity conditions and existence theorems in nonlinear elasticity. *Archive for Rational Mechanics and Analysis*, 63:337–403, 1976.
- [4] C. G. Broyden. A class of methods for solving nonlinear simultaneous equations. *Mathematics of Computation*, 19(92):577–593, 1965.
- [5] G. F. Carey. *Computational Grids: Generation, Adaptation, and Solution Strategies*. Taylor and Francis, Washington, DC, 1997.
- [6] A. S. Dvinsky. Adaptive grid generation from harmonic maps on Riemannian manifolds. *Journal of Computational Physics*, 95:450–476, 1991.
- [7] R. Fletcher and M. J. D. Powell. A rapidly convergent descent method for minimization. *The Computer Journal*, 6(2):163–168, 1963.
- [8] E. Hairer and G. Wanner. *Solving Ordinary Differential Equations II: Stiff and Differential-Algebraic Problems*. Springer, Berlin, 2 edition, 1996.
- [9] W. Huang. Practical aspects of formulation and solution of moving mesh partial differential equations. *Journal of Computational Physics*, 171:753–775, 2001.
- [10] W. Huang. Variational mesh adaptation: Isotropy and equidistribution. *Journal of Computational Physics*, 174:903–924, 2001.
- [11] W. Huang. Metric tensors for anisotropic mesh generation. *Journal of Computational Physics*, 204:633–665, 2005.
- [12] W. Huang and L. Kamenski. A geometric discretization and a simple implementation for variational mesh generation and adaptation. *Journal of Computational Physics*, 301:322–337, 2015.
- [13] W. Huang and L. Kamenski. On the mesh nonsingularity of the moving mesh PDE method. Technical Report WIAS Preprint 2218, Weierstrass Institute for Applied Analysis and Stochastics, Berlin, 2016.
- [14] W. Huang and R. D. Russell. *Adaptive Moving Mesh Methods*. Springer, New York, 2010.
- [15] W. Huang and W. Sun. Variational mesh adaptation II: Error estimates and monitor functions. *Journal of Computational Physics*, 184:619–648, 2003.
- [16] Y. Huang, Y. Su, H. Wei, and N. Yi. Anisotropic mesh generation methods based on ACVT and natural metric for anisotropic elliptic equation. *Science China Mathematics*, 56(12):2615–2630, 2013.
- [17] D. A. Knoll and D. E. Keyes. Jacobian-free newton-krylov methods: a survey of approaches and applications. *Journal of Computational Physics*, 193(2):357–397, 2004.
- [18] P. Knupp and S. Steinberg. *Fundamentals of Grid Generation*. CRC Press, Boca Raton, FL, 1993.
- [19] P. M. Knupp and N. Robidoux. A framework for variational grid generation: Conditioning the Jacobian matrix with matrix norms. *SIAM Journal on Scientific Computing*, 21:2029–2047, 2000.
- [20] A. Kolasinski and W. Huang. A new functional for variational mesh generation and adaptation based on equidistribution and alignment conditions. *Computers and Mathematics with Applications*, 75:2044–2058, 2018.
- [21] H. G. Lee, K. Kim, and J. Kim. On the long time simulation of the Rayleigh–Taylor instability. *International Journal for Numerical Methods in Engineering*, 85(13):1633–1647, 2011.

- [22] R. Li, T. Tang, and P. Zhang. Moving mesh methods in multiple dimensions based on harmonic maps. *Journal of Computational Physics*, 170:562–588, 2001.
- [23] J. A. Mackenzie and W. Mekwi. On the use of moving mesh methods to solve PDEs. *Journal of Computational Physics*, 214:1–17, 2006.
- [24] J. Nocedal and S. J. Wright. *Numerical Optimization*. Springer, New York, 2 edition, 2006.
- [25] J.-F. Remacle, X. Li, M. S. Shephard, and J. E. Flaherty. Anisotropic adaptive simulation of transient flows using discontinuous Galerkin methods. *International Journal for Numerical Methods in Engineering*, 62:899–923, 2005.
- [26] J. Shen and X. Yang. An efficient moving mesh spectral method for the phase-field model of two-phase flows. *Journal of Computational Physics*, 228:2978–2992, 2009.
- [27] H. Tang and T. Tang. Adaptive mesh methods for one- and two-dimensional hyperbolic conservation laws. *SIAM Journal on Numerical Analysis*, 41:487–515, 2003.
- [28] T. Tang. Moving mesh methods for computational fluid dynamics. In Z. C. Shi, Z. Chen, T. Tang, and D. Yu, editors, *Recent Advances in Adaptive Computation*, volume 383 of *Contemporary Mathematics*, pages 141–173. American Mathematical Society, Providence, RI, 2005.
- [29] Y. V. Vassilevski, V. G. Dyadechko, and K. N. Lipnikov. Hessian-based anisotropic mesh adaptation in domains with discrete boundaries. *Russian Journal of Numerical Analysis and Mathematical Modelling*, 20:391–408, 2005.
- [30] A. M. Winslow. Adaptive-mesh zoning by the equipotential method. Technical Report UCRL-73200, Lawrence Livermore National Laboratory, 1981.
- [31] Y. Zheng, H. Wei, Y. Huang, C. Chen, T. Tian, H. Liu, W. Wang, and L. He. FEALPy v3: A cross-platform intelligent numerical simulation engine. *arXiv preprint*, 2025.